OpenFOAM® Journal

Volume 5 [Full Papers], Pages 59–89
ISSN: 2753-8168

Development of an OpenFOAM® Solver to investigate the dynamic absorption and desorption processes in metal-hydrides

Christoph Ulrich*, Maximilian R. Ziegler, Daniel F. Szambien, Christian Buhl, and Roland Scharf

Institute for Power Plant Engineering and Heat Transfer, Gottfried Wilhelm Leibniz University Hannover, An der Universität 1, 30823 Garbsen, Germany
Email address: ulrich@ikw.uni-hannover.de

Email address: ziegler@ikw.uni-hannover.de

Email address: szambien@ikw.uni-hannover.de

Email address: buhl@ikw.uni-hannover.de

Email address: scharf@ikw.uni-hannover.de

DOI: https://doi.org/10.51560/ofj.v5.110
Results with version(s): OpenFOAM® v8
Repository: https://github.com/ChristophUlrichITV/twoRegionHydrideFoam

Abstract. The purpose of this paper is to introduce *twoRegionHydrideFoam*, a newly developed solver that enables the calculation of hydrogen absorption and desorption reactions in metal-hydrides. This solver integrates simulations of chemical, thermodynamic, and continuum mechanical processes. The primary focus is to provide a detailed, locally resolved description of hydrogen loading cycles under varying temperatures and pressures. We discuss the mathematical model assembled for this purpose and its implementation in OpenFOAM®. Additionally, precise heat transfer calculations are achieved using the groovyBC third-party library. The performance and accuracy of the solver are demonstrated through a parametric study where key system parameters are systematically varied and analyzed. Furthermore, this paper includes preconfigured example cases to facilitate understanding and application of the solver. This solver meets the increasing demand for advanced tools in sustainable energy storage and hydrogen technology research. By expanding the capabilities of OpenFOAM®, it offers a powerful platform for researchers and engineers to explore and develop innovative solutions within the hydrogen economy.

1. Introduction

1.1. **Motivation.** Global fossil fuel consumption has surged by 800 % over the past 70 years and has doubled since 1980 [1]. Energy demand is expected to grow by 1.6 % annually until 2030 [2]. This increase in energy demand, coupled with the rise in greenhouse gas emissions from fossil fuel use, underscores the urgent need to transition to renewable energy sources. Green hydrogen, in particular, holds significant promise as an energy carrier for the transportation sector and for generating electricity and heat. Although substantial research and development efforts have been made to harness hydrogen, further advancements are needed to ensure its safe storage.

Currently, hydrogen storage primarily relies on high-pressure tanks, operating within a pressure range of [300 bar $\leq p_{H_2} \leq$ 700 bar], or alternatively, its liquefied form. Both methods have high energy requirements and significant storage losses. Additionally, there are major safety concerns due to the potential for uncontrolled hydrogen release. In response, the authors are developing hydrogen tanks using an alternative storage method: binding hydrogen in special metals known as metal-hydrides. These storage systems offer advantages in terms of compactness, operation near ambient conditions, and adaptability to various temperature-pressure requirements. They provide inherent safety due to low system pressures and controlled hydrogen release [3]. However, they also have drawbacks, such as low gravimetric energy densities and complex process control. This complexity necessitates a thorough understanding of the thermodynamic and technical behavior of metal-hydrides. Effective heat dissipation and supply are

* Corresponding author

Received: 17 August 2023, Accepted: 10 February 2025, Published: 31 March 2025

crucial to ensure that charging and discharging times are within the desired range and that safe operation is maintained. To address these challenges, a mathematical model of the absorption and desorption reactions has been developed and implemented as a novel solver in OpenFOAM®.

We believe that metal-hydrides represent a significant advancement in the field of hydrogen storage. As research progresses, it is likely that a variety of innovative storage concepts will emerge. To facilitate greater accessibility and usability of metal-hydride simulations for the broader research community, we have implemented an established mathematical model of the absorption and desorption reactions as a novel solver within the OpenFOAM® framework. This development provides researchers and engineers with a powerful tool for conducting detailed simulations and further investigations into metal-hydride-based hydrogen storage systems.

1.2. **Introduction to Metal-Hydrides.** The term metal-hydrides encompasses metals, alloys, and intermetallic compounds capable of forming a chemical bond with hydrogen. In this study, examples include Hydralloy C5, which is primarily composed of manganese and titanium, as well as $LaNi_5$.[1] By applying thermal energy, hydrogen can be released from the metal-hydride [6].

$$\text{Metal } (M) + \text{Hydrogen } (H) \underset{\textbf{Desorption}}{\overset{\textbf{Absorption}}{\rightleftharpoons}} \text{Metal-Hydride } (MH) + \text{Thermal Energy} \tag{1}$$

During the loading process, gaseous hydrogen is initially adsorbed onto the metal's surface through physical adsorption. Under sufficient pressure, the hydrogen permeates the surface, diffuses into the lattice and forms a solid solution known as the α-phase, where hydrogen is randomly distributed within the metal lattice. As pressure increases, the hydrogen concentration also rises. However, due to attractive atom interactions, the α-phase reaches its maximum hydrogen storage capacity [5]. At this point, the β-phase begins to form, characterized by a higher hydrogen concentration (see Fig. 1 (A)). The Gibbs-Phase-Rule

$$F = C - P + 2 \tag{2}$$

can be applied, where $C = 2$ represents the number of components (Metal + Hydrogen) and $P = 3$ represents the number of phases (hydrogen gas + α-phase + β-phase). This rule determines the degree of freedom $F = 1$, corresponding to the thermodynamic temperature T. Under isothermic conditions, the degree of freedom becomes $F = 0$, and the conversion from metal to metal-hydride occurs at a constant pressure, known as the equilibrium pressure p_{eq}. The equilibrium pressure indicates the amount of reversibly storable hydrogen and the required operating pressure. The relationship between temperature and the corresponding pressure can be represented using pressure-concentration isotherms (PCI), which can be calculated using the Van't-Hoff equation

$$\ln(p) = \frac{\Delta H}{R\,T} - \frac{\Delta S}{R} \tag{3}$$

using p as the system pressure, ΔH as the enthalpy of formation, ΔS as the change in entropy during absorption/desorption, T as the thermodynamic temperature and R as the universal gas constant. By plotting the pressure plateaus logarithmically against the inverse temperature for each PCI, a material specific Van't-Hoff diagram is obtained (see Fig. 1 (A)). The gradient $(-\Delta H/R)$ can be used to determine the enthalpy of formation ΔH, which is particularly important for thermal management. It should be

[1]Further implementation and research was conducted on: MgH_2; MgNi; HWT5800; MmNiFe; MmNiAl.

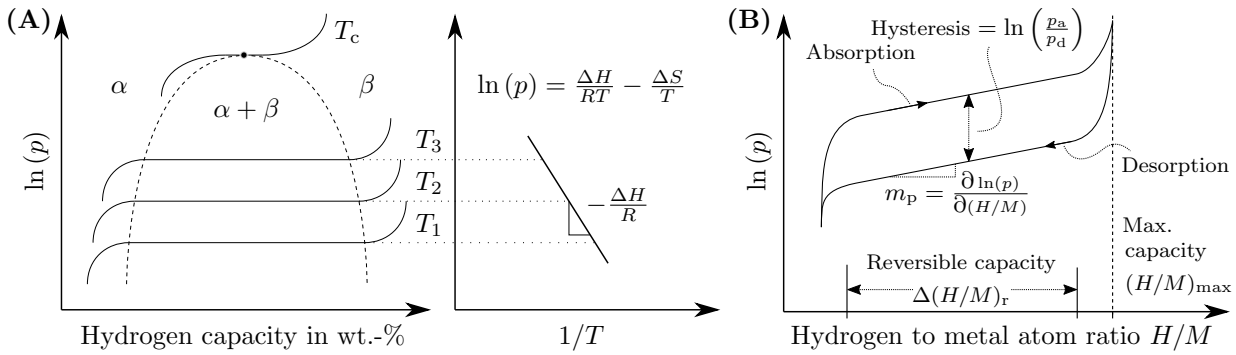

Figure 1. (A) PCI's and Van't-Hoff diagram – adapted from [4]; (B) Isothermal hysteresis loop – adapted from [4, 5]

noted that these idealized pressure-concentration-isotherms deviate from real storage processes (see Fig. 1 (B)).

1.2.1. *Slope of Pressure Plateaus.* Real metal-hydrides exhibit pressure plateaus with a slope (m_p). The material specific slope can be calculated by relating the rate of pressure change $\mathrm{d}\,(\ln p)$ to the change in absorbed hydrogen in terms of number of atoms $\mathrm{d}\,(H/M)$ or in mass percent $\mathrm{d}\,(\omega_\mathrm{H})$:

$$m_\mathrm{p} = \frac{\mathrm{d}\,(\ln p)}{\mathrm{d}\,(n_\mathrm{H}/n_\mathrm{M})} = \frac{\mathrm{d}\,(\ln p)}{\mathrm{d}\,(H/M)} \qquad \text{or} \qquad m_\mathrm{p} = \frac{\mathrm{d}\,(\ln p)}{\mathrm{d}\,(m_\mathrm{H}/m_\mathrm{M})} = \frac{\mathrm{d}\,(\ln p)}{\mathrm{d}\,(\omega_\mathrm{H})} \tag{4}$$

The slope can vary between absorption and desorption, often fluctuating significantly during both processes. The quality of the metal-hydride is crucial, as material inhomogeneity and surface characteristics play a substantial role in these variations.

1.2.2. *Hysteresis.* Hysteresis refers to the difference in pressure level between absorption and desorption pressure plateaus. During the cyclic charging and discharging of metal-hydrides, a hysteresis loop occurs.

1.2.3. *Reversible Capacity.* The technically utilizable amount of storable hydrogen in a tank is known as the reversible capacity [$\Delta\,(H/M)_\mathrm{r}$ or $\Delta\,(\omega_\mathrm{H})_\mathrm{r}$]. This reversible capacity is significantly lower than the maximum capacity [$\Delta\,(H/M)_\mathrm{max}$ or $\Delta\,(\omega_\mathrm{H})_\mathrm{max}$]. Storage tank design parameters, such as pressure and temperature ranges, must be considered as limiting factors.

1.3. **State of the Art in Metal-Hydride Simulations.** In recent years, significant advancements have been made in the numerical simulation of hydrogen absorption and desorption by metal-hydrides. Various models have been developed with the objective of improving the understanding of the kinetics, thermodynamics, and heat transfer processes involved in these systems. However, we have identified several limitations and assumptions in existing literature that impact the accuracy and scalability of these simulations. We will outline these issues in the following paragraphs.

1.3.1. *Container Geometries with Limited Customization.* A review of the relevant literature reveals that numerous geometric representations employed in computer-simulated models lack customizability and frequently fail to reflect the characteristics of their real-world counterparts [7–11]. This is particularly apparent when modeling small, intricate storage tanks. Such limitations can adversely affect the dependability of simulations and the anticipated expenditures when transferring from laboratory settings to industrial applications. Our investigation indicates that using commercially available pipes for storage tanks could provide significant advantages in such scenarios.

1.3.2. *Neglect of Outer Wall Influence.* A common assumption is that the storage vessel walls can be treated as adiabatic or infinitely thin [7, 9, 12–22]. However, in reality, these walls have finite thickness and specific thermal properties, and may even include surface modifications such as fins, which can significantly impact heat transfer dynamics. Ignoring these factors can lead to inaccurate predictions of the system's thermal behavior. This issue is addressed by using heat transfer equations that account for the reactor walls, thereby modeling their impact accurately. While the surface modifications can be implemented using the groovyBC library, this falls outside the scope of the present paper.

1.3.3. *Oversimplification of Heat Transfer Mechanism.* Many models simplify the heat transport mechanisms by using gradient-based approaches, which do not fully capture the complexities of real heat transfer processes [7, 9, 14–16, 18, 20, 21, 23–26]. These simplified assumptions may overlook critical factors, such as convective heat transfer and non-linear thermal gradients within the storage vessels walls. As a result, such simplifications can lead to significant discrepancies between predicted and actual performance, particularly under dynamic operation conditions.

1.3.4. *Disregarding Heat Transfer through the Hydrogen Inlet.* It is often overlooked that the hydrogen inlet can act as either a source or sink for thermal energy [7,9,10,12,18,20,21,25,27]. The heat dissipated by the hydrogen gas plays a crucial role in the system's overall thermal management and should not be underestimated. Ignoring this factor can lead to an underestimation of cooling requirements and an inaccurate prediction of the system's overall performance.

1.3.5. *Omitting Expansion Volumes and Filters.* The expansion volume above the metal-hydride bed is frequently treated as a free space, overlooking the presence of filters [7, 9, 10, 14, 18–23, 27, 28]. These filters, which are installed to prevent particle migration, have significantly higher thermal conductivity compared to metal-hydrides. As a result, they should be incorporated into simulations. Neglecting to account for filters can lead to incorrect assumptions about heat distribution and thermal management within the system. To address this issue, a boundary condition has been implemented at the hydrogen inlet.

2. Numerical Model

The storage and release of hydrogen in real metal-hydride-based storage tanks are investigated numerically. A mathematical model is assembled to describe the reactions (see Eqn. 1). To approximate the complex transient behavior inside a metal-hydride based storage tank, the following assumptions are made in the mathematical model:

(1) Hydrogen behaves as an ideal gas;
(2) The temperature and pressure of hydrogen at the inlet are uniform and constant;
(3) The volumetric expansion of the metal-hydride is negligible;
(4) The metal-hydride powder forms an isotropic, homogeneous, and constant-porosity packed bed;
(5) The properties of the metal-hydride remain constant during hydrogen absorption and desorption;
(6) Heat radiation and gravitational force are negligible.
(7) Local thermal equilibrium exists between metal-hydride and hydrogen;

By incorporating these assumptions, the processes in metal-hydride-based storage tanks can be described using the principles of mass, momentum and energy conservation [7–9, 23, 26, 29–32].

2.1. **Conservation of Mass.** For the metal, the conservation of mass can be described by[2]

$$(1-\varepsilon)\,\frac{\partial \rho_\mathrm{s}}{\partial t} = S_{\mathrm{m},i} \tag{5}$$

and for hydrogen by:

$$\varepsilon \frac{\partial \rho_\mathrm{g}}{\partial t} + \nabla \cdot (\rho_\mathrm{g} \mathbf{u}_\mathrm{g}) = -S_{\mathrm{m},i} \tag{6}$$

In Eqns. (5,6), the porosity of the metal powder bed ε, the specific density ρ_g and the velocity vector of the hydrogen $\mathbf{u}_\mathrm{g}$ are utilized. Both equations describe the change in density during the reaction. The term $S_{\mathrm{m},i}$ represents a source term for absorption

$$S_{\mathrm{m,a}} = C_\mathrm{a} \cdot \exp\left(-\frac{E_{\mathrm{A,a}}}{R\,T}\right) \cdot \ln\left(\frac{p}{p_{\mathrm{eq,a}}}\right) \cdot (\rho_{\mathrm{s,sat}} - \rho_\mathrm{s}) \tag{7}$$

or a sink term for desorption

$$S_{\mathrm{m,d}} = C_\mathrm{d} \cdot \exp\left(-\frac{E_{\mathrm{A,d}}}{R\,T}\right) \cdot \left(\frac{p - p_{\mathrm{eq,d}}}{p_{\mathrm{eq,d}}}\right) \cdot (\rho_\mathrm{s} - \rho_{\mathrm{s,emp}}) \tag{8}$$

depending on the system pressure, temperature, and the level of stored hydrogen [19, 33, 34].[3] Given that no reaction can occur in the hydrogen/filter region, the local source term is zero ($S_{\mathrm{m},i} = 0$). Both equations consist of three terms to describe the reaction kinetics and thus the rate of hydrogen absorption or desorption:

(1) The Arrhenius equation incorporates a specific reaction speed constant C_i, the activation energy $E_{\mathrm{A},i}$, the universal gas constant R, and the thermodynamic temperature T;
(2) The comparison between the prevailing hydrogen pressure p and the equilibrium pressure of the metal-hydride $p_{\mathrm{eq},i}$;
(3) The saturation level, which is determined by matching the current loading ρ_s to either the saturated state $\rho_{\mathrm{s,sat}}$ or the empty state $\rho_{\mathrm{s,emp}}$.

Several approaches can be employed to determine the equilibrium pressure $p_{\mathrm{eq},i}$ of metal-hydrides. One approach is to utilize the Van't-Hoff equation, which involves the enthalpy ΔH and entropy ΔS of reaction:

$$p_{\mathrm{eq,a}} = p_{\mathrm{eq,d}} = p_\mathrm{ref} \cdot \exp\left(\frac{\Delta H}{R\,T} - \frac{\Delta S}{R}\right) \tag{9}$$

One notable drawback of this approach is its disregard for the loading of the metal. Therefore, it is advisable to employ a more accurate method, such as utilizing polynomial equations. For instance, when

[2]Indices: s solid, g gaseous, i case indicator (a absorption, d desorption), sat saturated, emp empty
[3]The differentiation mechanism between absorption and desorption is the subject of Sec. 4.4.

considering Hydralloy C5 within the temperature range of $[0\,^\circ\mathrm{C} \leq \vartheta \leq 100\,^\circ\mathrm{C}]$, the equation for the absorption reaction can be expressed as follows:

$$\begin{aligned}\frac{p_{\mathrm{eq,a}}}{p_{\mathrm{ref}}} =& \exp\left(a_1 + \frac{a_2}{T} + a_3 T + a_4 \omega_{\mathrm{H}}^{\alpha} + a_5 \omega_{\mathrm{H}} + a_6 \omega_{\mathrm{H}}^2 + a_7 \omega_{\mathrm{H}}^3 + a_8 \omega_{\mathrm{H}}^4\right) \\ &+ \exp\left(b_1 + b_2 \omega_{\mathrm{H}} + b_3 T + b_4 T^2 + b_5 T^3\right)\end{aligned} \tag{10}$$

Similarly, the equation for the desorption reaction is expressed as:

$$\begin{aligned}\frac{p_{\mathrm{eq,d}}}{p_{\mathrm{ref}}} =& \exp\left(a_1 + \frac{a_2}{T} + a_4 \omega_{\mathrm{H}}^{\alpha} + a_5 \omega_{\mathrm{H}} + a_6 \omega_{\mathrm{H}}^2 + a_7 \omega_{\mathrm{H}}^3 + a_8 \omega_{\mathrm{H}}^4\right) \\ &+ \exp\left(b_1 + b_2 \omega_{\mathrm{H}} + b_3 T + b_6 \frac{\omega_{\mathrm{H}}}{T}\right)\end{aligned} \tag{11}$$

a_i, b_i, α are coefficients determined empirically [7].[4] According to Manai [27], the mass percent of absorbed hydrogen ω_{H} (see Eqn. 4) can be determined by:

$$\omega_{\mathrm{H}} = \frac{\rho_{\mathrm{s}} - \rho_{\mathrm{s,emp}}}{\rho_{\mathrm{s,emp}}} \cdot 100 \tag{12}$$

To characterize the percentage of absorbed hydrogen in the metal, the conversion (or reacted fraction) Z can be determined by utilizing the initial mass percent of absorbed hydrogen $\omega_{\mathrm{H},0}$[5] and the technically saturated state $\omega_{\mathrm{H,sat}}$.

$$0 \leq Z \leq 1, \qquad Z = \begin{cases} \dfrac{\omega_{\mathrm{H}} - \omega_{\mathrm{H},0}}{\omega_{\mathrm{H,sat}}} & \text{Absorption} \\ 1 + \dfrac{\omega_{\mathrm{H}} - \omega_{\mathrm{H},0}}{\omega_{\mathrm{H,sat}}} & \text{Desorption} \end{cases} \tag{13}$$

For the absorption of $LaNi_5$, the polynomial function, utilizing the coefficients a_i is expressed as follows:

$$p_{\mathrm{eq,a}} = p_{\mathrm{ref}} \cdot \exp\left(\frac{\Delta H_{\mathrm{a}}}{R\,T_{\mathrm{ref}}} - \frac{\Delta S}{R}\right) = \left[a_0 + \sum_{i=1}^{7} a_i \left(\frac{H}{M}\right)^i\right] \cdot \exp\left[\frac{\Delta H_{\mathrm{a}}}{R}\left(\frac{1}{T} - \frac{1}{T_{\mathrm{ref}}}\right)\right] \tag{14}$$

And for the desorption:

$$p_{\mathrm{eq,d}} = \left[a_0 + \sum_{i=1}^{9} a_i \left(\frac{H}{M}\right)^i\right] \cdot \exp\left[\frac{\Delta H_{\mathrm{d}}}{R}\left(\frac{1}{T} - \frac{1}{T_{\mathrm{ref}}}\right)\right] \tag{15}$$

The ratio of hydrogen to metal atoms, denoted as H/M (see Eqn. 4) can be determined using the methods described in references [3, 9, 29]

$$\frac{H}{M} = \frac{2 \cdot (\rho_{\mathrm{s}} - \rho_{\mathrm{s,emp}})}{M_{\mathrm{g}}} \cdot \frac{M_{\mathrm{s}}}{\rho_{\mathrm{s,emp}}} \tag{16}$$

using the molar masses of hydrogen (M_{g}) and metal-hydride (M_{s}). Moreover, the saturated density of the metal can be determined by:

$$\rho_{\mathrm{s,sat}} = \rho_{\mathrm{s,emp}} \cdot \left(1 + \frac{\omega_{\mathrm{H,sat}}}{100}\right) \tag{17}$$

A middle ground between the Van't-Hoff equation and the polynomial equations is the Van't-Hoff relationship

$$p_{\mathrm{eq}} = p_{\mathrm{ref}} \cdot \exp\left(A - \frac{B}{T}\right) \tag{18}$$

with material constants A and B derived from experimental data [8, 17, 24, 35].

2.2. **Conservation of Momentum.** To simplify the conservation of momentum in the pipe, we assume a laminar flow of hydrogen, where Darcy's-Law

$$\mathbf{u} = -\frac{K}{\mu_{\mathrm{g}}} \nabla p \tag{19}$$

can be applied due to the porous nature of all regions within the tank. Here, K represents the permeability of the packed bed and

$$\mu_{\mathrm{g}} = 9.05 \cdot 10^{-6} \cdot \left(\frac{T/\mathrm{K}}{293}\right)^{0.68} \tag{20}$$

[4] For a full list of coefficients see Tab. A.1 in the Appendix.

[5] $\omega_{\mathrm{H},0}$ (absorption) $< \omega_{\mathrm{H},0}$ (desorption); define which reaction you want to start with in `constant/metalHydrideSettings`

the dynamic viscosity of hydrogen [20,27]. By combining Eqn. 19 with the conservation of mass in Eqn. 6 and the Ideal-Gas-Law

$$\rho_{\mathrm{g}} = \frac{p\, M_{\mathrm{g}}}{R\, T} \tag{21}$$

the conservation of momentum can be rewritten as follows:

$$\varepsilon \frac{M_{\mathrm{g}}}{R\, T}\left(\frac{\partial p}{\partial t} - \frac{p}{T}\frac{\partial T}{\partial t}\right) = \frac{K}{\mu_{\mathrm{g}}}\nabla\cdot(\rho_{\mathrm{g}}\nabla p) - S_{\mathrm{m},i} \tag{22}$$

This equation provides the time-sensitive rate of change in hydrogen pressure $\partial p/\partial t$ used to calculate the hydrogen pressure in the next time step [8, 19, 20, 27, 36]. Subsequently, the pressure difference between adjacent cells is calculated and inserted into Darcy's Law (see Eqn. 19).

2.3. **Conservation of Energy.** Assuming local thermal equilibrium between the hydrogen and the packed bed or filter, it is possible to use

$$(\rho c_p)_{\mathrm{eff},j}\frac{\partial T}{\partial t} + \nabla\cdot(\rho_{\mathrm{g}}\, c_{p,\mathrm{g}}\, \mathbf{u}\, T) = \nabla\cdot(k_{\mathrm{eff},j}\,\nabla T) + S_{\mathrm{m},i}\cdot\left[\frac{\Delta H}{M_{\mathrm{g}}} - T\,(c_{p,\mathrm{g}} - c_{p,\mathrm{s}})\right] \tag{23}$$

to describe the temperature field. The mass source/sink term is zero for the hydrogen filter area, because no reactions occur in this region. The porosity-weighted effective heat capacity $(\rho c_p)_{\mathrm{eff},j}$ of the metal-hydride and hydrogen filter areas (see Fig. 2) is calculated as follows:

$$(\rho c_p)_{\mathrm{eff,MH}} = \varepsilon\,\rho_{\mathrm{g}}\, c_{p,\mathrm{g}} + (1-\varepsilon)\,\rho_{\mathrm{s}}\, c_{p,\mathrm{s}} \tag{24}$$

$$(\rho c_p)_{\mathrm{eff,filterArea}} = \varepsilon_{\mathrm{filter}}\,\rho_{\mathrm{g}}\, c_{p,\mathrm{g}} + (1-\varepsilon_{\mathrm{filter}})\,\rho_{\mathrm{filter}}\, c_{p,\mathrm{filter}} \tag{25}$$

The effective thermal conductivity $k_{\mathrm{eff},j}$ is determined by:

$$k_{\mathrm{eff,MH}} = \varepsilon\, k_{\mathrm{g}} + (1-\varepsilon)\, k_{\mathrm{s}} \tag{26}$$

$$k_{\mathrm{eff,filterArea}} = \varepsilon_{\mathrm{filter}}\, k_{\mathrm{g}} + (1-\varepsilon_{\mathrm{filter}})\, k_{\mathrm{filter}} \tag{27}$$

3. Initial and Boundary Conditions

At the start of a simulation, the initial conditions are assumed to be in thermodynamic equilibrium[6]

$$t = t_0 \rightarrow \begin{cases} T(x,y,z,t_0) & = T_0 \\ \rho_{\mathrm{s}}(x,y,z,t_0) & = \rho_{\mathrm{s},0} \\ \rho_{\mathrm{g}}(x,y,z,t_0) & = \rho_{\mathrm{g},0} \\ \mathbf{u}(x,y,z,t_0) & = 0 \\ p(x,y,z,t_0) & = p_0 \end{cases} \tag{28}$$

as detailed Appendix B, along with their corresponding boundary conditions. All walls in the system are impermeable to mass transfer. Boundary values and the rationale for using the third-party library `groovyBC`, developed by Bernhard Gschaider [37], are provided in Sec. B.1.

4. Structure of the Solver

This section provides a comprehensive overview of the solver's structural and functional aspects. The description of the pipe geometries employed in the simulation is presented initially. Material parameters and the selection of the method for calculating equilibrium pressure are defined afterwards. Next, it covers the initialization of simulation parameters in the relevant files. The section then explains the solver's decision making process for absorption and desorption. A brief subsection addresses the implementation of conservation equations. The final part of the section focuses on meshing the different regions, including a detailed discussion of pressure and temperature exchange between these regions.

[6] In order to maintain readability, the dependence on the spatial coordinates and time will not be repeated. Spatially and time variable parameters are to be taken into account accordingly.

4.1. **Geometry Information.** The authors propose that future research should focus on scalable pressurized storage pipes. Pipes have been shown to possess optimal geometric properties for withstanding high pressures and facilitating effective heat transfer. To ensure optimal process control, a heat exchanger can be utilized to introduce or extract thermal energy through a moving medium on the exterior surface. This approach is applicable across various scales, from individual pipes to pipe-bundle heat exchangers. Both geometries include a porous filter at the hydrogen inlet and a packed bed of metal-hydride. One of these designs features an additional central gas channel made from the same filter material used at the inlet.

Two predefined `blockMesh` files are located in the `system` folder of the *template* case:

(1) *blockMeshDict_full*: Represents the filled pipe in Fig. 2a.
(2) *blockMeshDict_hollow*: Represents the filled pipe + gas channel in Fig. 2b

For evaluation (see Secs.5.2 and 5.3.3), two Points, shown in Fig. 2a, are evaluated. Point A is located at (20 mm | 0 mm | 20 mm) while Point B is positioned at (20 mm | 0 mm | 50 mm) in a pipe with the length of 110 mm, a diameter of 48.3 mm, and a simulated wall thickness of 1.06 mm.

To optimize computational time, the pipe's axial symmetry is leveraged by using a wedge-shaped mesh (see Fig. 2c). To simulate a specific pipe configuration, a section named *config* is inserted at the beginning of the corresponding `blockMesh` file. This section is then converted into vertices through inline calculations.

In the `blocks` sub-dictionary, it is crucial to correctly name the mesh regions for the metal-hydride area (*metalArea*) and the hydrogen/filter area (*hydrogenArea*).[7] These explicit names are used by the solver during mesh initialization (as defined in *createMeshes.H*) and calculation. The two regions represent the distinct areas required by the solver for accurate simulation.

4.2. **Material Definition.** The *hydrideMaterialConfig* file in the `constant` folder functions as a database, defining all material parameters required for the simulation. The current entries in this file are based on literature references.[8]

The selection of a specific material is made in the *metalHydrideSettings* file. Here, the heat transfer parameters must be re-entered and should match the values specified in *hydrideMaterialConfig*. Furthermore, four different methods of pressure calculation can be chosen:

(1) Van't-Hoff-Equation (Eqn. 9)
(2) Polynomial equation for Hydralloy C5 (Eqns. (10,11))
(3) Polynomial equation for $LaNi_5$ (Eqns. (14,15))
(4) Van't-Hoff-Relationship (Eqn. 18)

[7] To ensure clarity, the mesh regions are referred to as *metalArea* and *hydrogenArea* for convenience, although it should be noted that these regions may not consist exclusively of the corresponding substances

[8] The compiled information is taken from [3,7,11,12,18,24,31,38–49] and is referred to in the source code at the corresponding lines

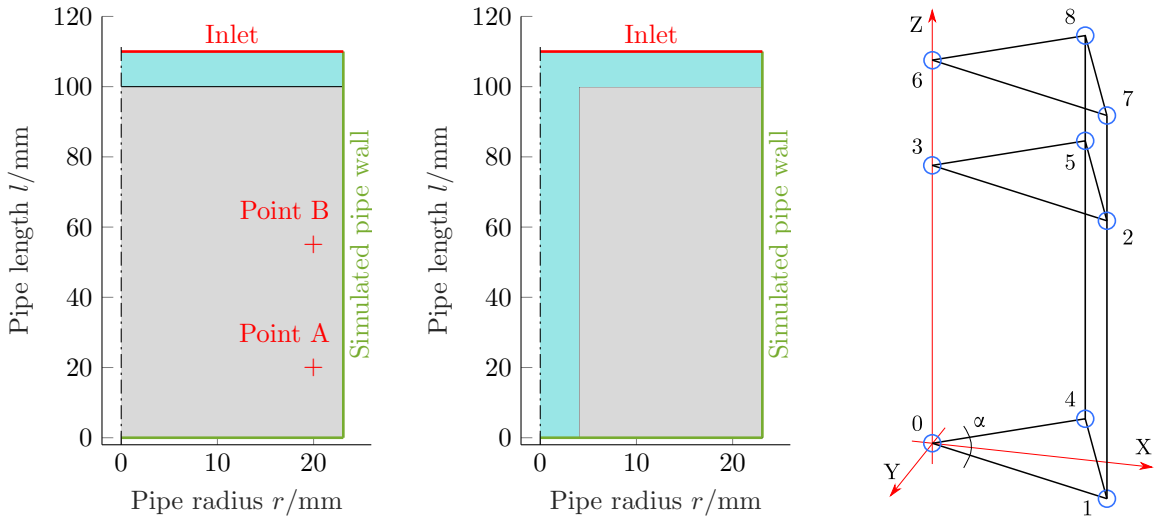

(a) Filled pipe **(b)** Filled pipe + gas channel **(c)** Wedge-geometry of (A)

Figure 2. Model geometries used – metal-hydride in gray and hydrogen/filter in blue

To facilitate troubleshooting and case setup correction, the output of intermediate results during simulation can be enabled by using *myDebugControl*. This feature helps identify and rectify any inaccuracies in the setup.

4.3. **Initialization of Simulation Parameters.** The function responsible for reading parameters is implemented in *readDictionaries.H*. It reads material parameters from *hydrideMaterialConfig* and *metalHydrideSettings*, then passes these parameters to the solver for further processing. To initialize the field variables, the files *createMetalFields.H* and *createHydrogenFields.H*, located in their respective mesh region folders, are used.

initializeHydrideProperties.H serves as a central location for initializing constants, constant field variables, and starting values. This includes the absorption/desorption constants for the polynomial equilibrium pressure calculations (see Tab. A.1 in Appendix A).

4.4. **Detection of Absorption / Desorption Reaction.** In *p_eq.H*, the determination of whether an absorption or desorption reaction occurs is made individually for each cell in the *metalArea*. The equilibrium pressure p_{eq} is calculated according to the specifications set in *metalHydrideSettings*. In *simulationControl.H*, the pressure of each cell is compared with the equilibrium pressures for absorption and desorption, as outlined in Listing 1:

(1) $p_i > p_{\mathrm{eq,a},i} \rightarrow$ absorption
(2) $p_i < p_{\mathrm{eq,d},i} \rightarrow$ desorption
(3) $p_{\mathrm{eq,d},i} \leq p_i \leq p_{\mathrm{eq,a},i} \rightarrow$ no reaction

Based on these calculation, support variables such as *absorptionAllowed* and *desorptionAllowed* are configured. These auxiliary variables enable the equations to be adjusted to include or exclude specific terms depending on whether absorption or desorption is permitted in a particular cell, thereby ensuring accurate modeling of the reactions and their impact on the system.

```
1  forAll(p, i)
2  {
3      if (p[i] > p_eq_a[i])
4      {   calcHelp_abs[i] = Foam::log(p[i] / p_eq_a[i]);
5          calcHelp_des[i] = 0;
6          absorptionAllowed[i] = 1;
7          desorptionAllowed[i] = 0;
8      }
9      else if (p[i] < p_eq_d[i])
10     {   calcHelp_abs[i] = 0;
11         calcHelp_des[i] = ((p[i] - p_eq_d[i])/p_eq_d[i]);
12         absorptionAllowed[i] = 0;
13         desorptionAllowed[i] = 1;
14     }
15     else
16     {   absorptionAllowed[i] = 0;
17         desorptionAllowed[i] = 0;
18         calcHelp_abs[i] = 0;
19         calcHelp_des[i] = 0;
20     }
21 }
```

Listing 1. Determination of the auxiliary variables in simulationControl.H

4.5. **Implementation of Conservation Equations.** The implementation of the conservation equations is organized by mesh regions, with each region having its own dedicated file. This structure is illustrated in Listing 2 using Eqn. 5 as an example. In line 4 of this code example, the control of the source and sink terms is demonstrated through the use of auxiliary variables.

```
1  fvScalarMatrix rhoMetalEqn(
2       (1-epsilon) * fvm::ddt(rhoMetal)
3      ==
4       Sm_a * absorptionAllowed + Sm_d * desorptionAllowed
5       );
```

Listing 2. Metal density calculation in *rhoMetalEqn.H*

4.6. **Coupling of Mesh Regions.** Due to the use of separate meshes for the *metalArea* and *hydrogenArea*, different equations can be applied to each region, allowing for tailored material data such as porosity or thermal conductivity. However, since the meshes operate in isolation, data exchange at their interfaces is necessary. Before the simulation begins, *collectFaces.H* identifies the shared interfaces between the meshes based on their hard-coded names. It is essential that the meshes adhere to the naming conventions specified in Sec. 4.1. The script then populates lists with cells adjacent to these interfaces. When the number of cells on both sides of an interface is equal, pairs of opposing cells are formed.[9] Pressure coupling is managed in *pressureTransfer.H*, as illustrated in Listing 3. This process involves transferring the pressure of the *hydrogenArea* cells to faces of the *metalArea* cells, ensuring that the pressure, which is imposed at the inlet, is properly propagated throughout the *metalArea*.

```
1    forAll (metalToHydrogenPatch, facei)
2    {
3        label IDCellHydrogen = patchCellsHydrogenToMetalPatch[facei];
4
5        p_hydrogen.boundaryFieldRef()[hydrogenToMetalPatchID][facei] =
6            p_hydrogen[IDCellHydrogen];
7        p.boundaryFieldRef()[metalToHydrogenPatchID][facei] =
8            p_hydrogen[IDCellHydrogen];
9     }
```

Listing 3. Pressure transfer from *hydrogenArea* to *metalArea* in *pressureTransfer.H*

In the simulation, determining the direction of cell temperature transfer between cells is not straightforward, complicating the temperature coupling process. To account for the heat released or absorbed due to reaction, the energy conservation equation for the *metalArea* is solved at each time step. The script *T_toHydrogen.H* handles the transfer of temperature values from the *metalArea* cells to the boundaries of the *hydrogenArea* cells as illustrated in Listing 4. Using these updated boundary values, the energy conservation equation is then solved for the *hydrogenArea*. Finally, the temperature values from the *hydrogenArea* cells are transferred back to the boundaries of the cells in the *metalArea*, completing the temperature coupling process, as shown in Listing 5. This iterative approach ensures that temperature values in both the *metalArea* and *hydrogenArea* are accurately updated, reflecting the heat transfer and reactions occurring in the system. For a clearer understanding, a solver flowchart is provided in Fig. 3.

```
1    forAll (metalToHydrogenPatch, facei)
2    {
3        label IDCellMetal = patchCellsMetalToHydrogenPatch[facei];
4
5        T_hydrogen.boundaryFieldRef()[hydrogenToMetalPatchID][facei] =
6                  T[IDCellMetal];
7    }
```

Listing 4. Temperature transfer from *metalArea* to *hydrogenArea* in *T_toHydrogen.H*

[9]This applies to all meshes discussed in this paper. For meshes with an uneven distribution of cells, the coupling process will need to be adjusted accordingly

```
1     forAll (metalToHydrogenPatch, facei)
2     {
3         label IDCellHydrogen = patchCellsHydrogenToMetalPatch[facei];
4
5         T_hydrogen.boundaryFieldRef()[hydrogenToMetalPatchID][facei] =
6           T_hydrogen[IDCellHydrogen];
7     }
```

Listing 5. Temperature transfer from *hydrogenArea* to *metalArea* in *T_toMetal.H*

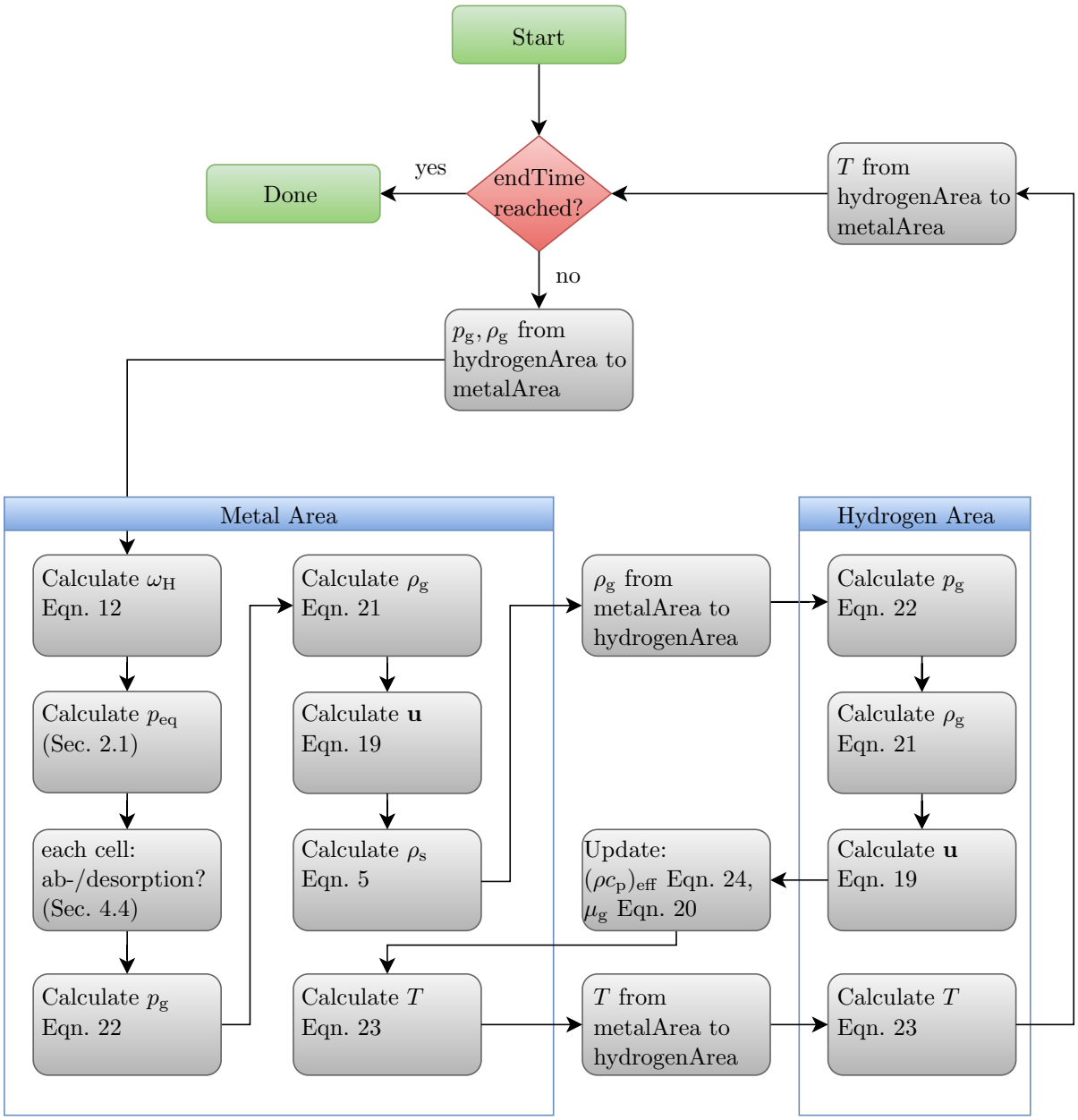

Figure 3. Flowchart of the solver's algorithm

5. Evaluation

5.1. **Pressure Propagation Analysis.** To substantiate the assumption of laminar flow and applicability of Darcy's Law, twelve simulations were conducted with varying pressure settings. In six simulations, the propagation of hydrogen pressure in the filter area was modeled (see Figs. 4a and 2b). In the remaining simulations, the hydrogen pressure in the filter area was assumed to be uniform and constant (see Fig. 4b). The results show that the simulated gas propagation inside the filter area cannot be accurately

modeled during the first second of the simulation. However, the simulated particle[10] Reynolds number for times greater than 0.8 s remained within the valid range of Darcy's-Law of $Re_{\mathrm{p,max}} = 1 \ldots 10$ [50–53].

It is important to note that in practical applications, an immediate pressure change $\Delta p_{\mathrm{H_2}}$ from $p_0 = 0.1\,\mathrm{MPa}$ to $p_{\mathrm{in}} = 4\,\mathrm{MPa}$ is unlikely and represents a theoretical scenario. Therefore, the required compliance with $Re_{\mathrm{p,max}} < 10$ for technically reasonable simulations is maintained.

In the simulations with constant pressure in the filter area, the particle Reynolds number only exceeds $Re_{\mathrm{p,max}} = 10$ during the first few milliseconds for the largest pressure increase to $p_{\mathrm{in}} = 4\,\mathrm{MPa}$. These results demonstrate that Darcy's law effectively describes the gas velocity for the operating conditions considered in this study. This finding is consistent with the sources previously referenced [7,10,12,14,17, 18,20,23,24]. It is important to note that different charging pressures are used for various metal-hydrides. For example, an inlet pressure of approximately 0.5 MPa is typical for $LaNi_5$, which significantly reduces the particle Reynolds number, as shown in the accompanying diagrams.

When comparing different pipe geometries, the propagation of hydrogen and its associated gas pressure significantly influences the conversion rate. Simulating the pressure propagation from the inlet and applying a constant gas pressure throughout the entire *hydrogenArea*, with varying step sizes, allows us to assess simulation accuracy against increased computing time and numerical instabilities.

[10] In this context, the term *particle* refers to an individual powder grain that makes up the packed bed of the metal-hydride

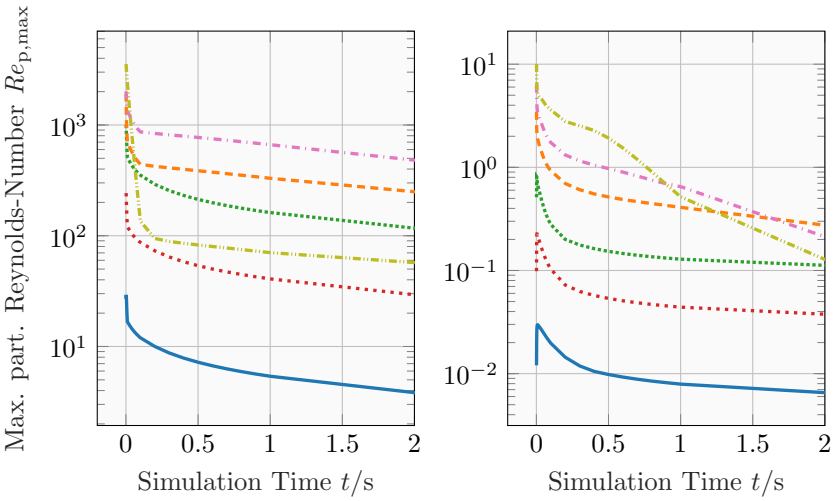

(a) Simulated gas pressure propagation inside the filter area (left) and its impact on the metal-hydride area (right)

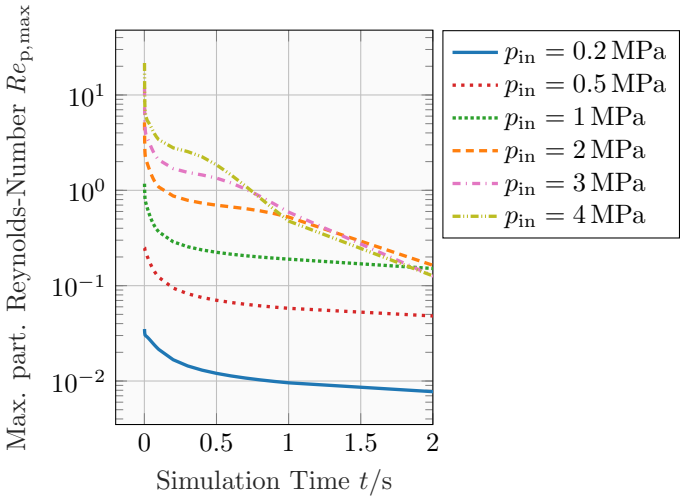

(b) Constant gas pressure in filter area and its effect on metal-hydride area

Figure 4. Maximum particle Reynolds numbers $Re_{\mathrm{p,max}}$

The impact of pressure propagation varies with the pipe's internal geometry. In the storage pipe without a gas channel (see Fig. 2a), the effect on the *hydrogenArea* at the inlet was found to be relatively minor. Conversely, in the storage pipe with a central gas channel (refer to Fig. 2b), the effect was more pronounced, but resulted in considerably increased calculation time. Key points to consider are:

(1) Simulating hydrogen propagation helps to analyze the initiation of absorption/desorption processes.
(2) After the initial hydrogen propagation, the step size can be gradually increased.
(3) Calculation time can be optimized by assuming homogeneous and constant pressure.
(4) The discrepancy between simulated gas propagation and the assumption of an instantaneous increase in gas pressure is directly proportional to the length of the simulated storage pipe.

However, in this study, the influence of gas propagation is negligible due to small pipe geometries.

5.2. **Studies of Parameter.** To demonstrate and validate the solver, a series of parametric studies were conducted for the absorption and desorption processes of Hydralloy C5. The focus was on the following operational parameters:

- the initial temperature, T_0,
- the cooling temperature, T_∞
- the inlet pressure, p_{in}
- the heat transfer coefficient, h

Additionally, two material-specific parameters were considered:

- the packed bed porosity ε
- the packed bed permeability K

And one geometric parameter:

- the pipe's wall thickness δ_{W}

Parameters not varied in the individual analyses were set as follows:

- $T_0 = T_\infty = 293.15\,\text{K}$ for absorption and $T_0 = 293.15\,\text{K}$, $T_\infty = 340\,\text{K}$ for desorption
- $h = 500\,\text{W}/(\text{m}^2\,\text{K})$
- $p_{\text{in}} = 3\,\text{MPa}$ (absorption) or $p_{\text{in}} = 0.1\,\text{MPa}$ (desorption).

The evaluation was performed at point B, as introduced in Sec. 4.1. Results of this study are presented in Figs. 5 and 6 for absorption and Figs. 7 and 8 for desorption. The findings are consistent with those reported in [7, 8, 13, 16, 17, 23, 27, 32–34, 54].

5.2.1. ***Absorption Analysis.***

Influence of the Initial Temperature T_0 and Coolant Temperature T_∞ (Fig. 5a).

(1) The amount of hydrogen absorbed increases as the coolant temperature decreases [13, 23, 27, 54].
(2) Lower coolant temperatures reduce the equilibrium pressure $p_{\text{eq,a}}$ and extend the absorption phase [7, 16, 23, 32, 33].
(3) The rate of absorption is highly sensitive to temperature. Lower Temperatures result in a faster reaction rate [13, 23, 27, 54].
(4) Starting the reaction at a higher initial temperature and using a higher coolant temperature leads to a higher peak temperature during absorption [13, 23, 27].

Influence of the Hydrogen Inlet Pressure p_{in} (Fig. 5b).

(1) The amount of hydrogen absorbed by the metal-hydride rises with increasing inlet pressure [7, 13, 17, 23, 27, 32, 34].
(2) Higher pressures lead to a faster reaction rate and an increase in released heat [7,8,13,23,27,32,34].
(3) Increased pressure improves heat transport significantly [8, 13, 23, 27, 34].
(4) The cooling process occurs more rapidly at higher pressures, despite the higher peak temperature [8, 13, 23, 27, 34].

Influence of the Heat Transfer Coefficient h (Fig. 5c).

(1) The absorption rate is strongly influenced by the heat transfer coefficient [13, 27].
(2) A higher heat transfer coefficient improves the rate of hydrogen absorption [13, 27].
(3) Reaction speed increases proportionally with h and approaches a technical optimal level.
(4) The metal-hydride's poor thermal conductivity[11] limits internal heat transport.
(5) A higher heat transfer coefficient slightly reduces the peak temperature [13, 27].

[11] Hydralloy C5: $k = 1\,\text{W}/(\text{m}\,\text{K})$; LaNi_5: $k = 3.18\,\text{W}/(\text{m}\,\text{K})$

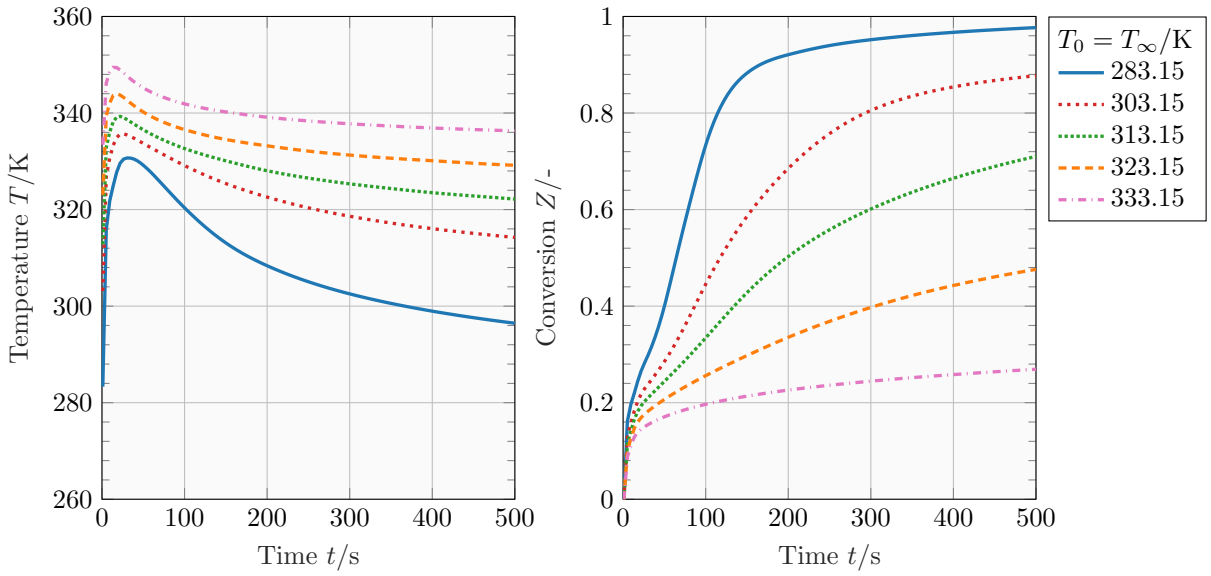

(a) Variation of initial temperature T_0 and coolant temperature T_∞

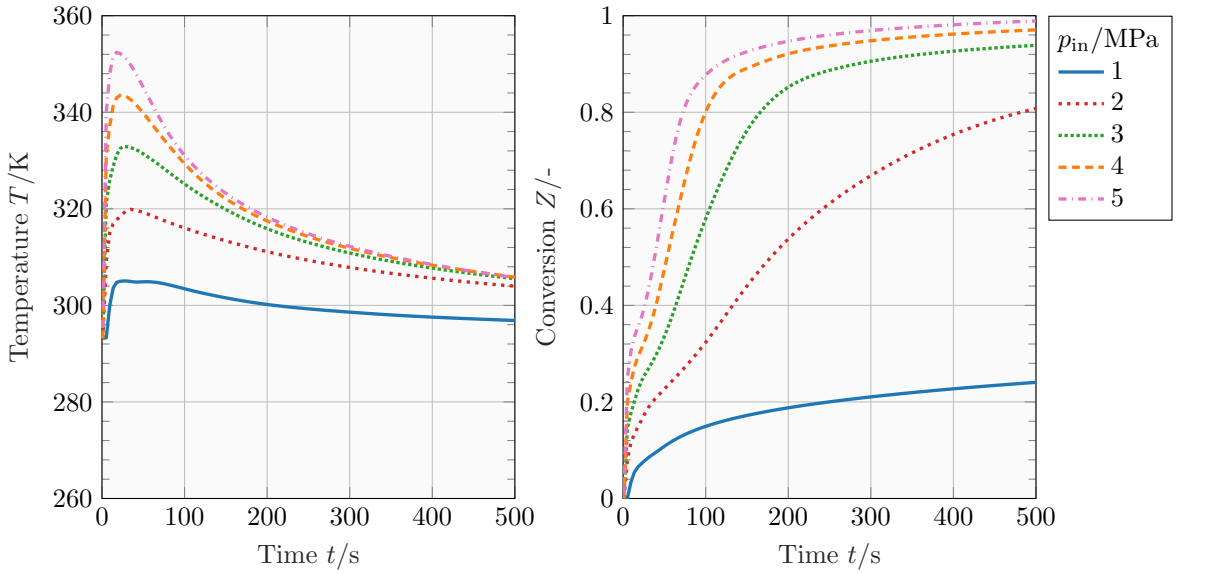

(b) Variation of hydrogen inlet pressure p_{in}

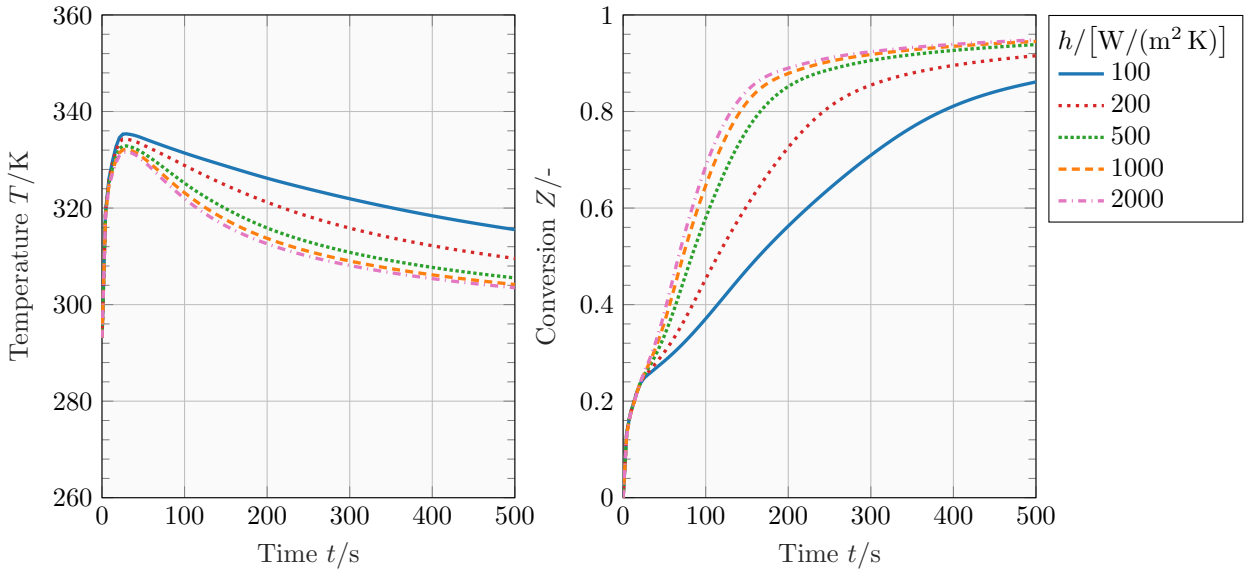

(c) Variation of heat transfer coefficient h

Figure 5. Simulated temperature T and conversion Z as a function of time and distinct parameter for Hydralloy C5 (absorption)

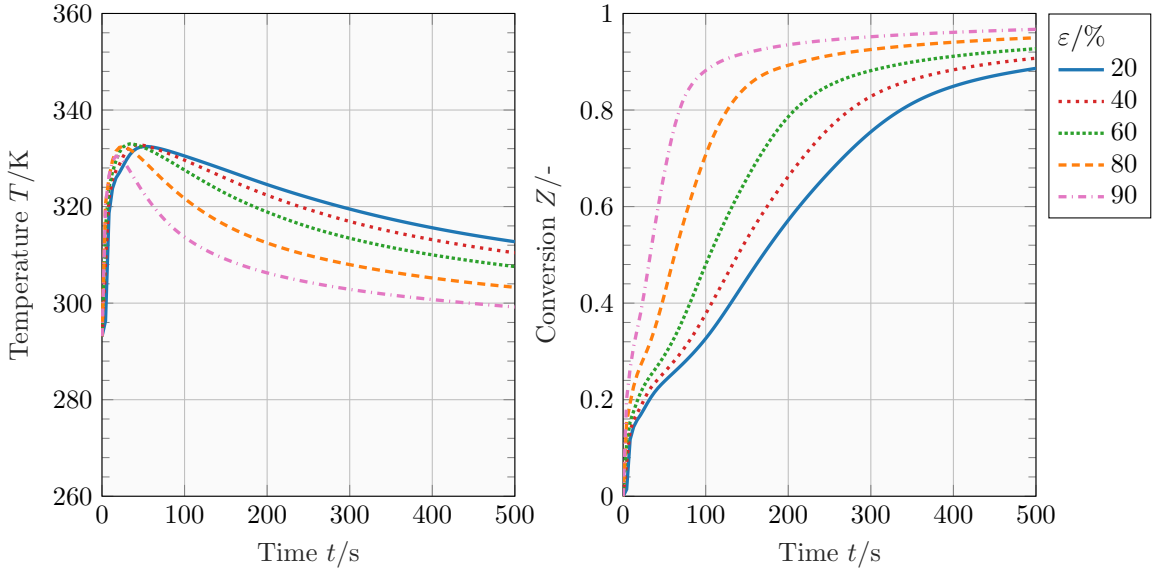

(a) Variation of the metal-hydride's porosity ε

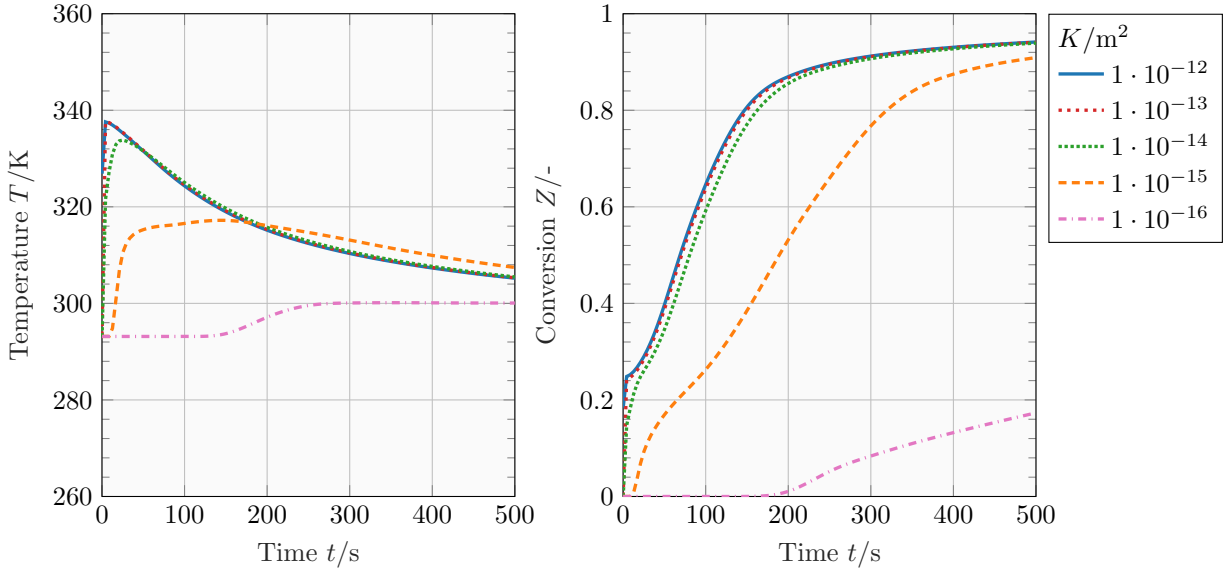

(b) Variation of the metal-hydride's permeability K

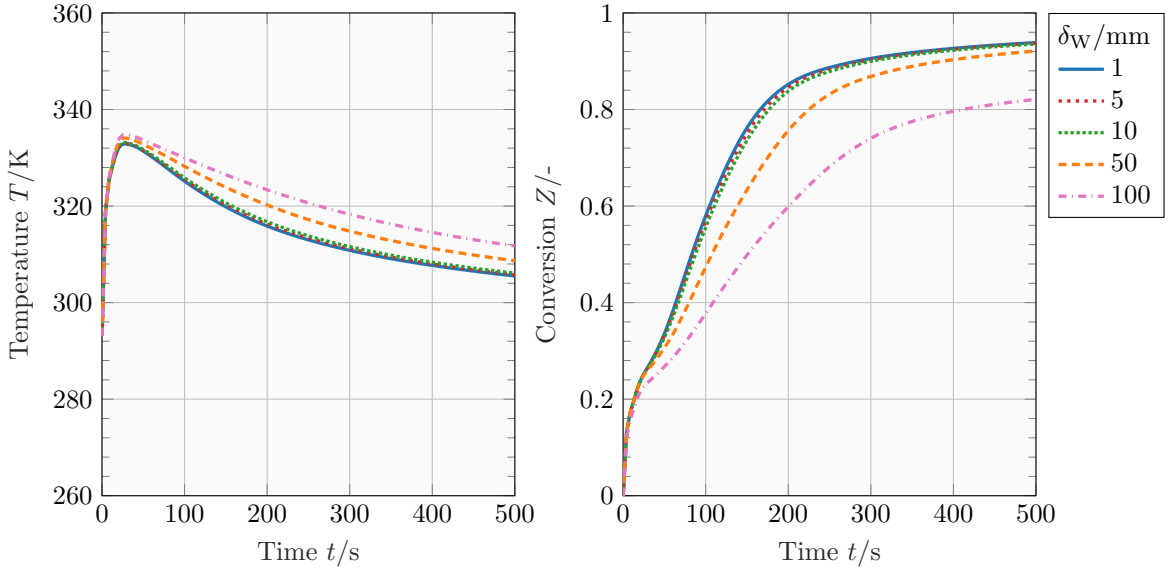

(c) Variation of the storage pipe's wall thickness δ_W

Figure 6. Simulated temperature T and conversion Z as a function of time and distinct parameter for Hydralloy C5 (absorption)

Influence of the Metal-Hydride's Porosity ε (Fig. 6a).

(1) Higher porosities result in a faster reaction speed and a slight reduction in maximum temperature [8, 34].
(2) Increased porosity significantly enhances cooling performance [34].
(3) Lower porosities extend the absorption phase [8, 34].
(4) Higher porosity reduces the overall capacity of the storage system.

Influence of the Metal-Hydride's Permeability K (Fig. 6b).

(1) Lower permeabilities drastically reduce the reaction speed.
(2) Higher permeabilities lead to an increase on the maximum temperature within the storage pipe.
(3) Permeability has no noticeable effect on cooling performance.
(4) Permeability does not have a significant impact on the amount of hydrogen absorbed.

Influence of the Pipe's Wall Thickness δ_{W} (Fig. 6c).

(1) For the examined wall material ($k = 21\,\mathrm{W/(m\,K)}$), variations in wall thickness within the practical range ($\delta_{\mathrm{W}} \leq 10\,\mathrm{mm}$) have a negligible effect on the absorption reaction
(2) Increasing the wall thickness leads to a higher maximum temperature within the storage pipe because heat dissipation is slower.
(3) The cooling performance remains unaffected by changes in wall thickness as long as the thickness remains within reasonable limits.
(4) Wall thickness does not significantly impact the amount of hydrogen absorbed.

5.2.2. ***Desorption Analysis.***

Influence of the Initial Temperature T_0 and Coolant Temperature T_∞ (Fig. 7a).

(1) The amount of desorbed hydrogen increases as the coolant temperature rises [23, 32, 54].
(2) Higher temperatures lower the equilibrium pressure $p_{\mathrm{eq,d}}$ and extend the desorption phase [23, 32, 54].
(3) The desorption rate is highly depending on temperature. Higher Temperatures accelerate the reaction speed [23, 32, 54].
(4) Starting the reaction at a higher initial and coolant temperature results in a reduction of the bottom temperature during desorption [23].

Influence of the Hydrogen Inlet Pressure p_{in} (Fig. 7b).

(1) The amount of hydrogen released by the metal-hydride rises with decreasing pressure [23].
(2) Higher inlet pressures lead to a slower reaction rate and an increase in heat absorption rate [23,32].
(3) Higher pressures significantly improve heat transport.
(4) Lower inlet pressures lead to a significantly stronger desorption reaction and thus to a significantly greater temperature drop at the start of the extraction process [23, 32].

Influence of the Heat Transfer Coefficient h (Fig. 7c).

(1) The desorption rate is strongly affected by the heat transfer coefficient [27].
(2) A higher heat transfer coefficient improves the rate of hydrogen desorption [27].
(3) Reaction speed increases proportionally with h, approaching a technically optimal level [27].
(4) The limiting factor for internal heat transport is the poor thermal conductivity of the metal-hydride.
(5) A lower heat transfer coefficient raises the minimum temperature in the storage system.

Influence of the Metal-Hydride's Porosity ε (Fig. 8a).

(1) Increasing the porosity results in a higher reaction rate [34].
(2) Lower porosities extend the desorption phase [34].
(3) Higher porosity decreases the capacity of the storage system (not shown in the graphs).

Influence of the Metal-Hydride's Permeability K (Fig. 8b).

(1) Lower permeabilities drastically decreases the reaction speed.
(2) Higher permeabilities significantly increase the minimum temperature in the storage pipe.
(3) Permeability has no observable effect on the heating performance.
(4) Permeability has a significant impact on the quantity of desorbed hydrogen.

Influence of the Pipe's Wall Thickness δ_W (Fig. 8c).

(1) For the examined wall material ($k = 21\,\mathrm{W/(m\,K)}$), variations in wall thickness within the practical range ($\delta_W \leq 10\,\mathrm{mm}$) have a minimal impact on the desorption reaction.
(2) Increasing the wall thickness results in a lower minimum temperature in the storage pipe.
(3) The wall thickness has minimal impact on the heat absorption process.
(4) The amount of desorbed hydrogen within the observed time frame is only slightly affected by the wall thickness, as long as it remains within a reasonable range.

5.3. **Additional Demonstration of the Solver's Capabilities.** In addition to the aforementioned parametric studies, the following three sub-sections highlight three key functionalities of the solver, namely:

(1) Selection of metal-hydrides by a comparison of absorption reactions of Hydralloy C5 and $LaNi_5$
(2) a comparison of pipe geometries, utilizing those presented in Sec. 4.1 in desorption reactions
(3) the cyclic loading and unloading of a storage pipe, comparing Hydralloy C5 and $LaNi_5$.

5.3.1. *Material Comparison via Absorption Reaction.* The behavior of Hydralloy C5 and $LaNi_5$ is compared, considering material-specific absorption pressures (Hydralloy C5: $p_{in} = 3\,\mathrm{MPa}$; $LaNi_5$: $p_{in} = 0.5\,\mathrm{MPa}$). The simulation results are illustrated in Fig. 9. It is crucial to avoid setting the starting hydrogen density too low, as this can result in inaccurate or incorrect equilibrium pressures due to the polynomial equations used.
Key observations:

- Initial Absorption Behavior:
  (1) After one second, distinct absorption behaviors are evident.
  (2) Hydralloy C5 exhibits a defined temperature profile.
  (3) $LaNi_5$ shows a temperature change across the entire metal-hydride bed, albeit significantly lower than that of Hydralloy C5.
- Reaction Dynamics:
  (1) Hydralloy C5 demonstrates a stronger and faster exothermic reaction.
  (2) Due to the higher loading pressure, Hydralloy C5 achieves a higher temperature and a greater amount of absorbed hydrogen.
- Core Formation:
  (1) After 100 seconds, the formation of a core region is observed for both temperature and conversion. This is a typical behavior for the absorption of hydrogen in metal-hydrides.
  (2) The equilibrium pressure increases with the amount of hydrogen absorbed and the thermal energy released during the absorption reaction.
  (3) Heat generated must first be dissipated via the container walls to the cooling medium so that the equilibrium pressure drops and further reaction can occur.
  (4) Consequently, the wall areas cool more rapidly than the central areas, resulting in a faster and/or prolonged reaction.

These findings are consistent with investigations conducted by Jiao [13], while other authors have examined $LaNi_5$ under longer time periods and higher hydrogen pressures [3, 9, 16, 25, 29, 33, 34, 54, 55].

5.3.2. *Geometry Comparison via Desorption Reaction.* Figure 10 illustrates the comparison of different inner pipe geometries (see Fig. 2) during desorption using Hydralloy C5. As the hydrogen pressure decreases, the desorption reaction begins. To fulfill the heat requirements of the reaction, the pipe is externally heated at a constant temperature of $T_\infty = 340\,\mathrm{K}$. The metal-hydride absorbs thermal energy, resulting in a temperature decrease along the pipe. This effect is further amplified by the presence of a central gas channel, where the pressure decreases more rapidly throughout the pipe. Consequently, hydrogen stored in the core of the pipe is released more quickly than in the completely filled storage pipe.

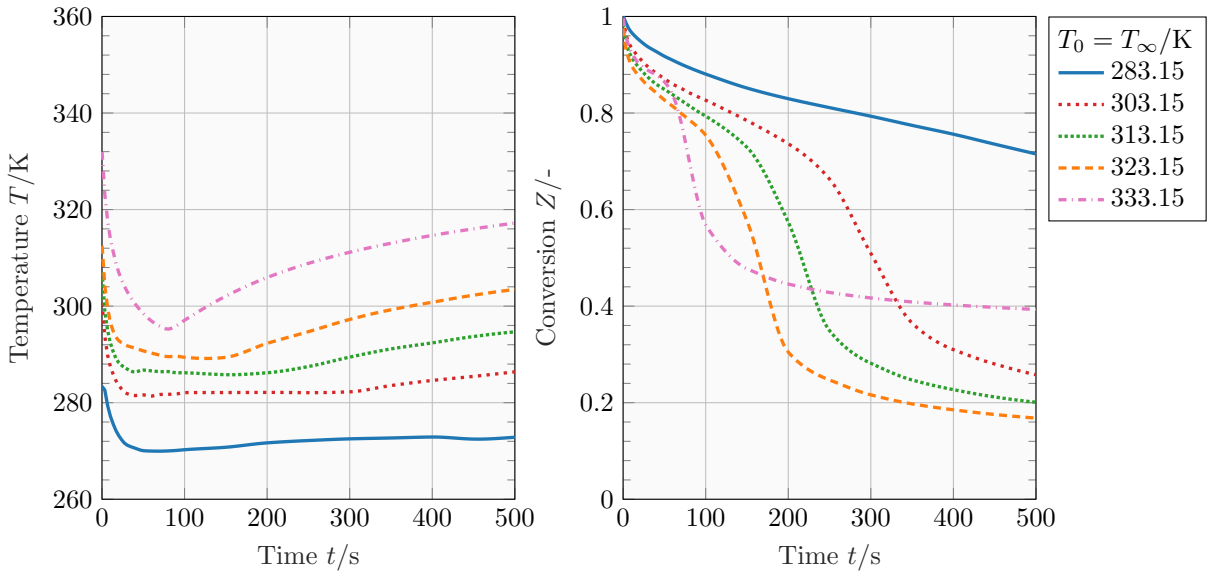

(a) Effect of initial temperature T_0 and coolant temperature T_∞

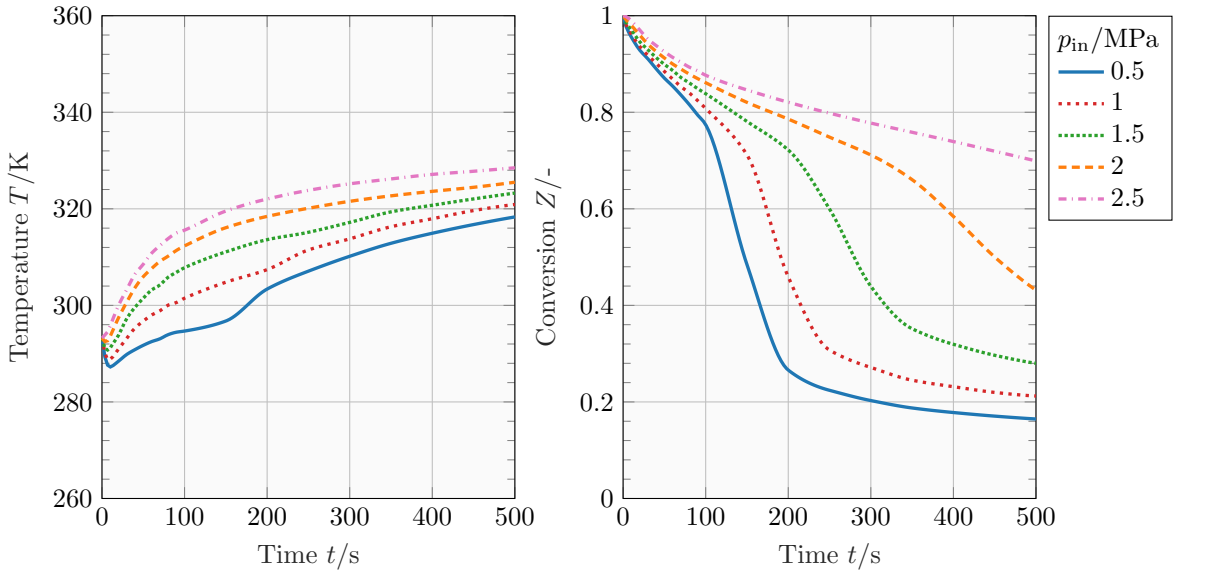

(b) Impact of hydrogen inlet pressure p_{in}

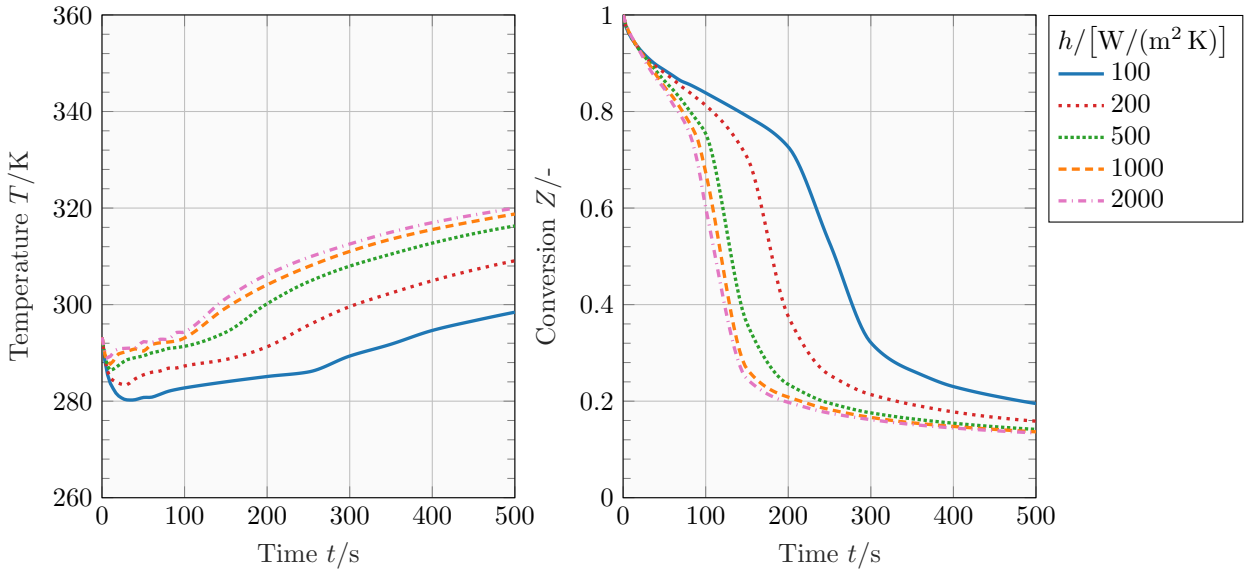

(c) Effect of heat transfer coefficient h

Figure 7. Simulated temperature T and Conversion Z as a function of time and distinct parameter for Hydralloy C5 (desorption)

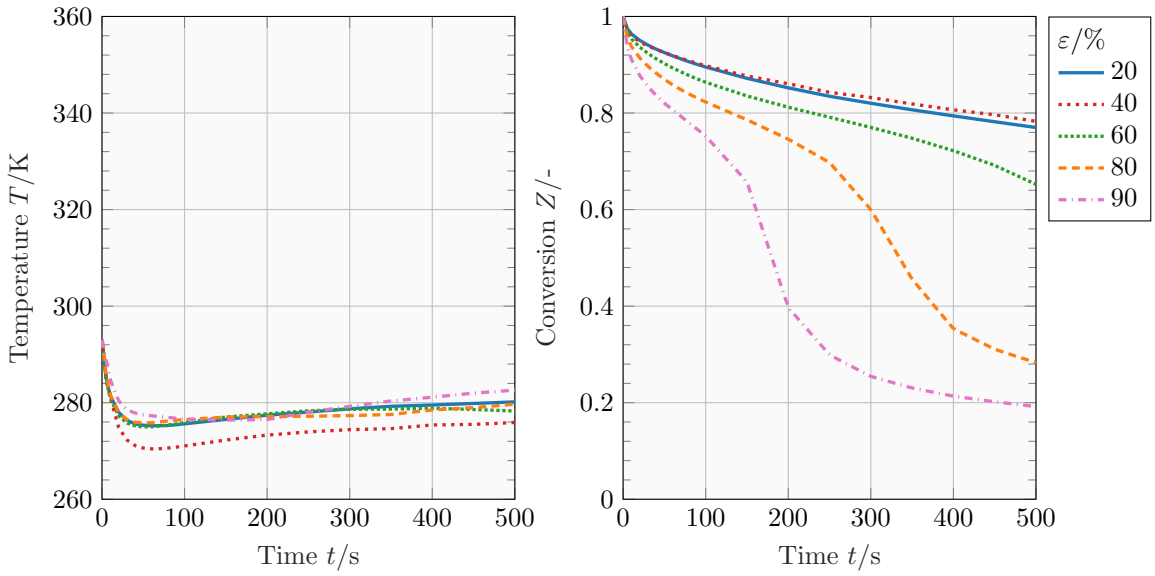

(a) Variation of the metal-hydride's porosity ε

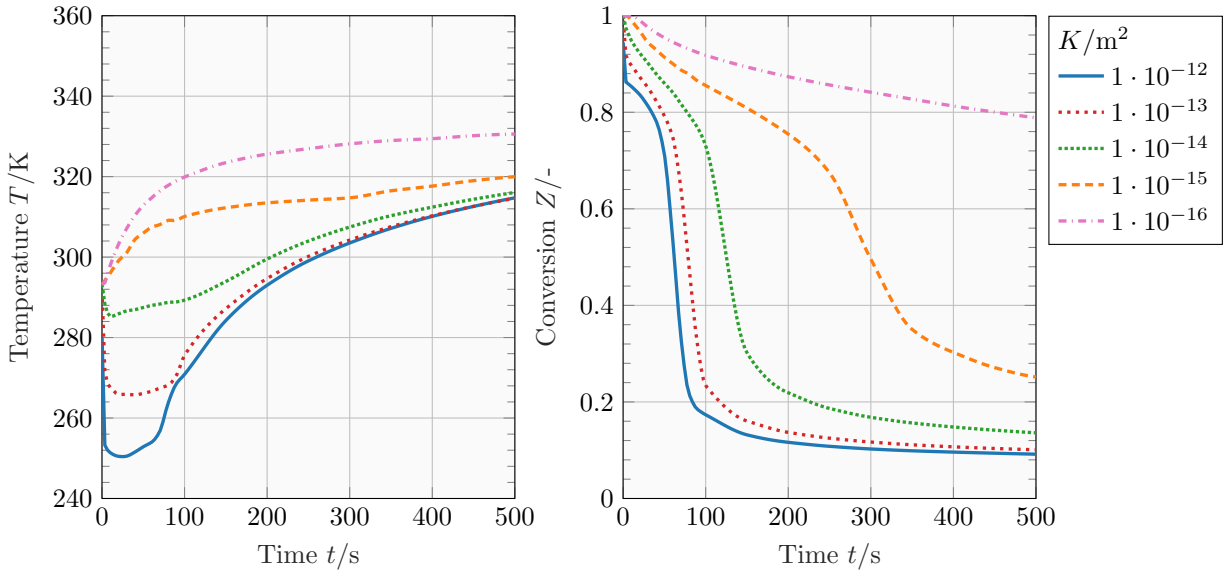

(b) Variation of the metal-hydride's permeability K

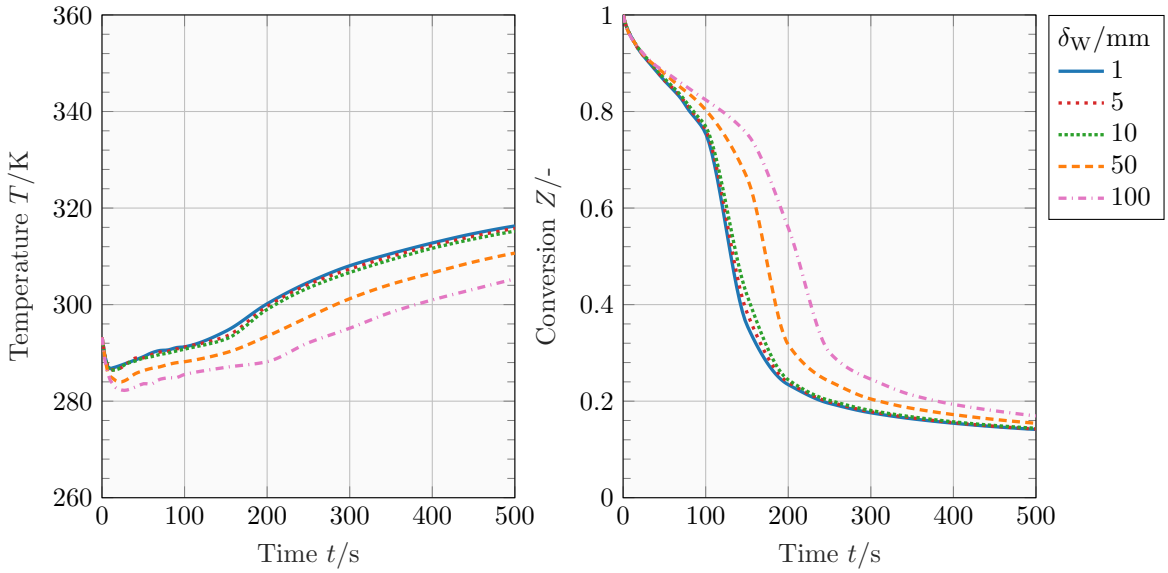

(c) Variation of the storage pipe's wall thickness δ_W

Figure 8. Simulated temperature T and Conversion Z as a function of time and distinct parameter for Hydralloy C5 (desorption)

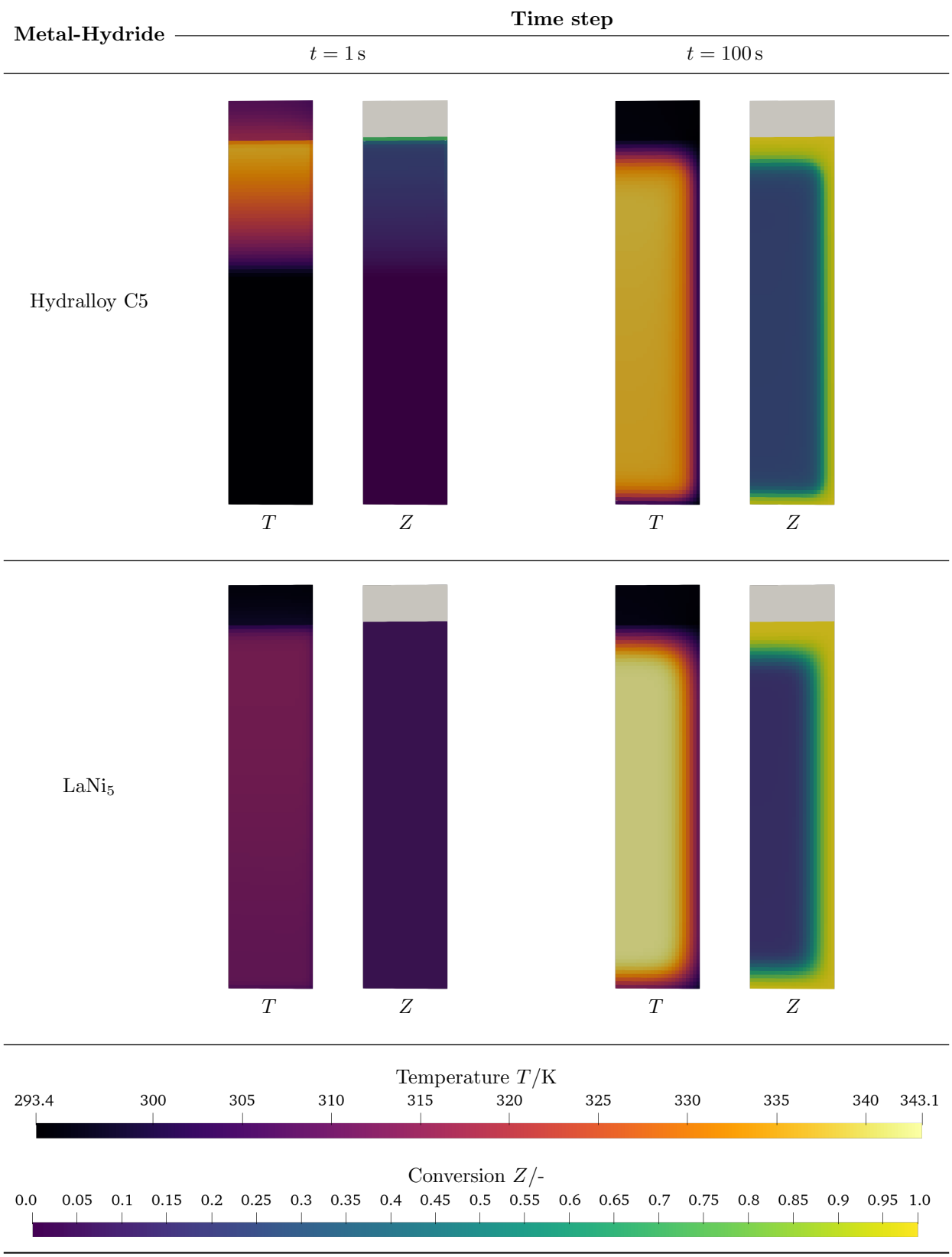

Figure 9. Absorption processes of Hydralloy C5 and $LaNi_5$;
Left: Temperature T/K; **Right:** Conversion Z;
Absorption pressures: 3 MPa (Hydralloy) & 0.5 MPa ($LaNi_5$)

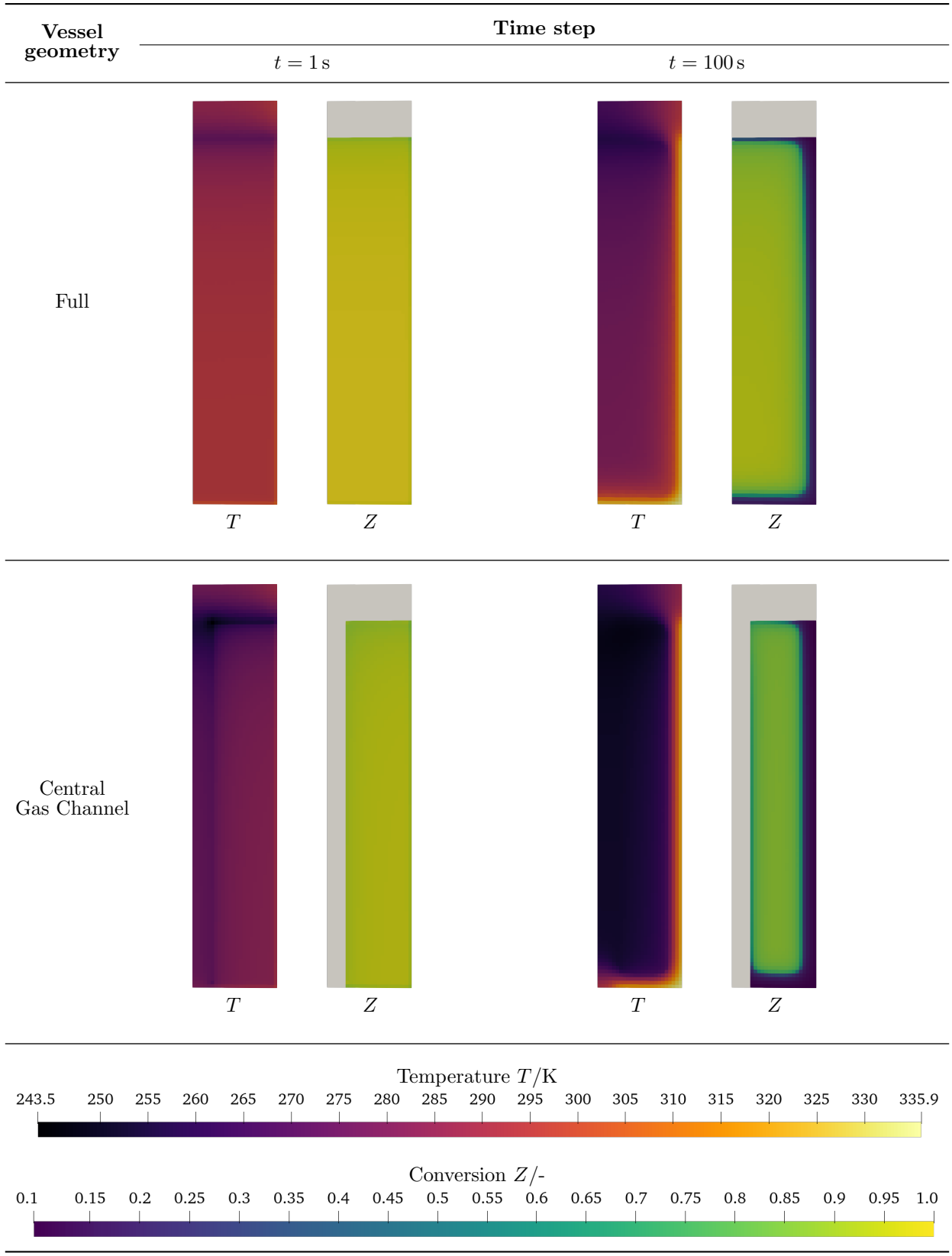

Figure 10. Desorption processes of Hydralloy C5 using different pipe geometries;
Left: Temperature T/K; **Right:** Conversion Z/-;
Desorption pressure: 0.1 MPa (both)

5.3.3. *Comparison of Cyclical Behavior.* An exemplary cycle is simulated for Hydralloy C5 and $LaNi_5$:

$$\text{Absorption} \xrightarrow{\textbf{200s}} \text{Desorption} \xrightarrow{\textbf{200s}} \text{Absorption} \xrightarrow{\textbf{200s}} \text{Desorption}$$

using the parameters seen in Tab. 1. Transitions between phases are instantaneous. The analysis focuses on two locations, Point A and Point B (see Fig. 2a), with results depicted in Fig. 11.

In the initial absorption phase described in Sec. 5.3.1, $LaNi_5$ exhibits a uniform hydrogen distribution due to a minimal pressure gradient, leading to a lower peak temperature, as shown in Fig. 5b. In contrast, Hydralloy C5 experiences a delayed absorption reaction because the hydrogen pressure takes longer to exceed the equilibrium pressure peq, a. This delay results in a significantly higher temperature due to Hydralloy C5's much larger absorption constant C_a ($6 \cdot 10^6\,\mathrm{s}^{-1}$ instead of $59.187\,\mathrm{s}^{-1}$). At 200 s, $LaNi_5$ reaches a higher conversion due to its lower maximum hydrogen saturation limit ($\omega_{\mathrm{H,sat}} = 1.3\,\%$) compared to Hydralloy C5's ($\omega_{\mathrm{H,sat}} = 1.8\,\%$). Additionally, greater porosity in Hydralloy C5 enhances cooling despite its lower thermal conductivity (Fig. 6a).

Desorption begins at 200 s with changes in hydrogen pressure and coolant temperature. Hydralloy C5 experiences a significant slowdown due to a sharp temperature drop, requiring heat conduction to the interior to accelerate the reaction. In contrast, $LaNi_5$ maintains a more stable reaction rate due to milder temperature and pressure drops and superior thermal conductivity. The behavior observed in the second absorption-desorption cycle is similar to that of the first.

Table 1. Parameters for comparative simulation of cyclical behavior

		Hydralloy C5	**$LaNi_5$**
Absorption Pressure	p_in	3 MPa	0.5 MPa
Desorption pressure	p_out	0.1 MPa	
Coolant temperature	T_∞	293.15 K	340 K
Heat transfer coefficient	h	$1000\,\mathrm{W/(m^2\,K)}$	

6. **Conclusion**

This paper presents `twoRegionHydrideFoam`, a newly developed solver for the thermodynamic analysis of metal-hydride absorption and desorption reactions within the OpenFOAM® framework. The solver employs a comprehensive mathematical model to determine system parameters including the density of metal-hydride and hydrogen, temperature, absorbed hydrogen, and control variables for each cell. This approach overcomes the limitations of simplified heat transfer at the boundary conditions often seen in the literature.

The solver's functionality has been rigorously evaluated through extensive parametric studies, aimed at validating its results against established literature. The comparison showed a strong correlation between the solver's performance and published findings, with no anomalies or errors detected in the examples tested.

This version of the solver includes polynomial equations specifically tailored for Hydralloy C5 and $LaNi_5$, while featuring general equations to accommodate other metal-hydrides. Its modular framework allows for future expansion to incorporate additional functionalities and materials. Analysis of metal-hydride degradation can be conducted by integrating further parameters into the solver.

The primary objective of this study is to provide the OpenFOAM®-Community with an advanced tool that supports research in metal-hydride-based hydrogen storage systems. As hydrogen storage research becomes increasingly crucial, this solver represents a significant advancement in the field.

Author Contributions: Conceptualisation, C.U. and M.R.Z.; methodology, C.U. and M.R.Z.; software, C.U.; validation, C.U., M.R.Z., R.S., D.F.S. and C.B.; formal analysis, C.U. and M.R.Z.; investigation, C.U., M.R.Z. and D.F.S.; resources, R.S. and C.U.; data curation, C.U.; writing—original draft preparation, C.U. and M.R.Z.; writing—review and editing, C.U., R.S., M.R.Z., D.F.S. and C.B.; visualisation, C.U.; supervision, M.R.Z. and R.S.; project administration, R.S. and M.R.Z.; funding acquisition, R.S. and D.F.S. and C.B.; All authors have read and agreed to the published version of the manuscript.

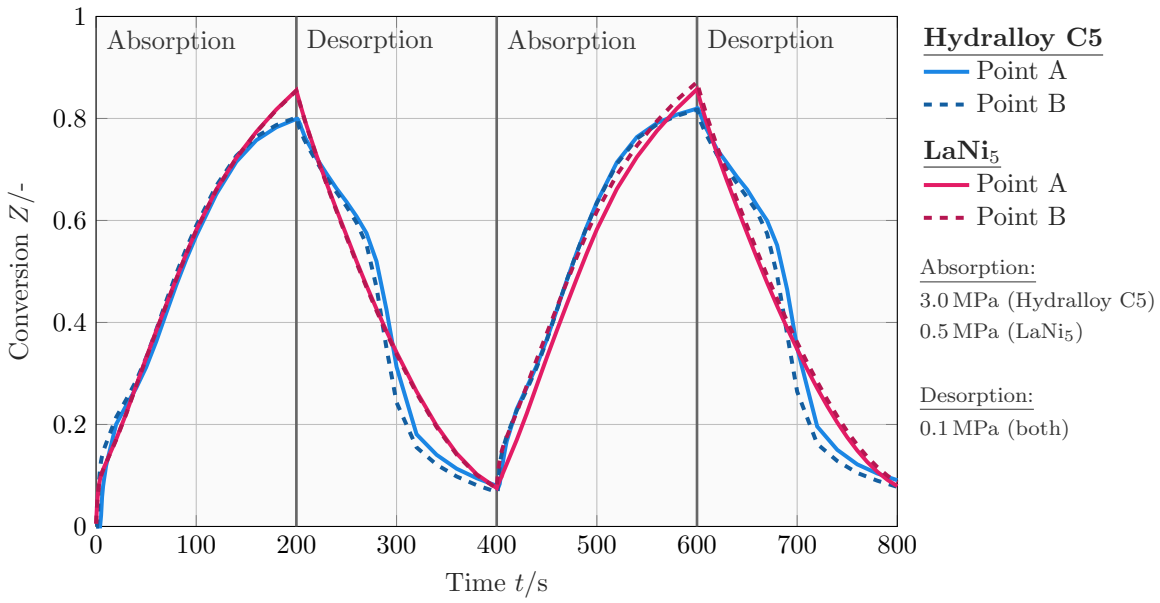

(a) Conversion Z

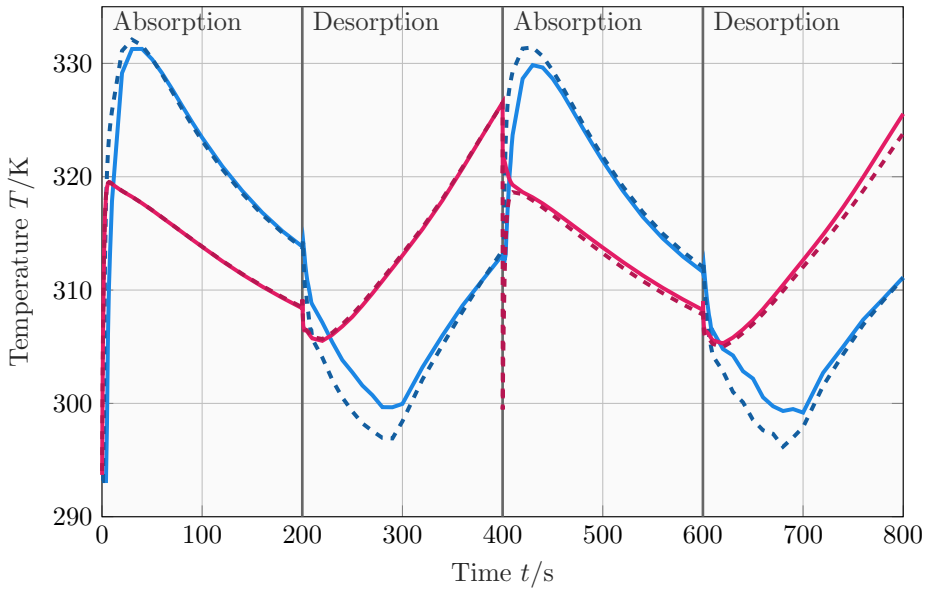

(b) Temperature T

Figure 11. Simulated temperature T and conversion Z for the cyclical behavior of Hydralloy C5 & $LaNi_5$

Appendix A. Coefficients for Equilibrium Pressure Calculation

Table A.1. Coefficients used to determine the equilibrium pressure for the absorption/desorption reaction (see Eqn. 10, Eqn. 11, Eqn. 14, Eqn. 15), taken from [3,7,9,29])

$LaNi_5$			Hydralloy C5		
Coefficient	**Absorption**	**Desorption**	**Coefficient**	**Absorption**	**Desorption**
a_0	−0.348 63	0.421	α	0.5	−0.3
a_1	10.1059	−4.114	a_1	−4.884	30.225
a_2	−14.2442	14.180	a_2	−2374.7	−3312.9
a_3	10.3535	−13.109	a_3	$3.4129 \cdot 10^{-3}$	-
a_4	−4.206 46	4.557	a_4	48.816	−10.078
a_5	0.962 371	0.166	a_5	−50.404	−14.603
a_6	−0.115 468	−0.592	a_6	22.711	12.889
a_7	0.005 637 76	0.179	a_7	−7.9717	−6.7934
a_8	-	−0.023	a_8	1.233	1.5872
a_9	-	$1.126 \cdot 10^{-3}$	b_1	−452.34	−59.282
			b_2	15.522	−4.7339
			b_3	4.0954	0.139 22
			b_4	$-1.3222 \cdot 10^{-2}$	-
			b_5	$1.4406 \cdot 10^{-5}$	-
			b_6	-	4743.7

Appendix B. Reasoning for Using groovyBC

In this section, we will explain the reasons for using groovyBC. Additionally, we will discuss the derivation of the equation used to simulate storage pipes, including their walls.

B.1. **Benefits of Using groovyBC.** The boundary values for a variable[12] $X = \{T, \rho_s, \rho_g, \mathbf{u}, p\}$ are determined by referencing the value at cell boundary X_{ref} to the value at the boundary X_B. This process accounts for the gradient $\nabla_{ref}(X)$ and the inverse distance from the cell center to the boundary patch $1/\delta$ [56]:

$$X_B = f \cdot X_{ref} + (1 - f) \cdot \left[X_X + \frac{\nabla_{ref}(X)}{1/\delta} \right] \tag{29}$$

Three different boundary conditions can be distinguished for partial differential equations, which are incorporated into the calculations using a weighted factor, denoted as f:

(1) The Dirichlet-boundary-condition ($f = 1$) provides function values.
(2) The Neumann-boundary-condition ($f = 0$) provides derivative values.
(3) The Robin-boundary-condition ($1 \geq f \geq 0$) provides both function and derivative values.

Since conditions can change during the simulation, it is necessary to continuously adjust the boundary values. To facilitate this, the third-party library *groovyBC*, developed by Bernhard Gschaider [37], was employed to handle heat conduction and convective boundary conditions. This library can read and evaluate field values of the mesh using user-defined functions, enabling stepwise adjustments of Eqn. 29. Furthermore, groovyBC can simulate a cross-flow heat exchanger by dividing the external temperature of the storage pipe into distinct temperature sections. This allows for the simulation of different processes by changing the boundary conditions.

Figure B.1 illustrates a general heat transfer scenario, encompassing heat transfer within the boundary cell and its adjacent wall, as well as convective heat transfer. By equating the corresponding heat fluxes, a mathematical description of the heat transfer phenomenon can be fomrulated:

$$\dot{q}_{conv} = \dot{q}_{cond,wall} = \dot{q}_{cond,cell} \rightarrow h\,(T_\infty - T_W) = \frac{k_W}{\delta_W}\,(T_W - T_B) = \frac{k_{eff}}{\delta}\,(T_B - T_X) \tag{30}$$

In Eqn. 30, h represents the heat transfer coefficient. However, since the external wall is not meshed, the temperature T_W is not included in the computational domain and must be determined using a general

[12]Indices: W ≙ outer wall, B ≙ inner wall/boundary, X ≙ cell center, ∞ ≙ free stream, ref ≙ referencing

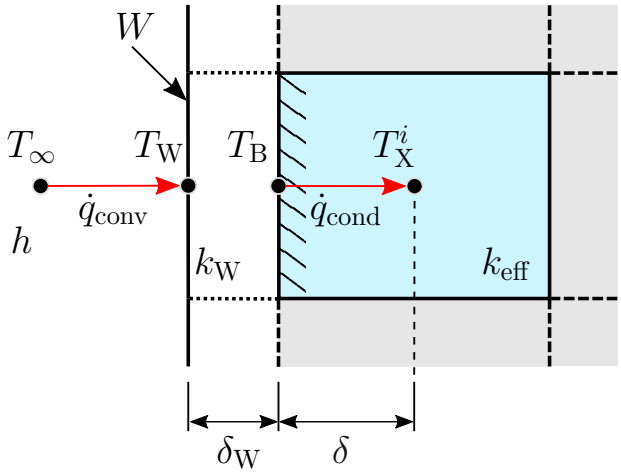

Figure B.1. Convective heat transfer through a boundary cell and an external wall – adapted from [56]

relation

$$\dot{q} = \frac{T_1 - T_2}{R_{1,2}} = \frac{T_2 - T_3}{R_{2,3}} \rightarrow \dot{q} = \frac{T_1 - T_3}{R_{1,3}} \quad \text{with} \quad R_{1,3} = R_{1,2} + R_{2,3} \tag{31}$$

that incorporates the thermal resistance R [56, 57]. By isolating T_B from Eqn. 30 and applying this relation, we obtain:

$$T_B = \frac{1}{1+\beta} \cdot T_\infty + \frac{\beta}{1+\beta} \cdot T_X \quad \text{with} \quad \beta = \frac{k_{eff}}{\delta} \cdot \frac{k_W + h\,\delta_W}{k_W\,h} \tag{32}$$

When comparing the commonly used gradient approach

$$-k_{eff}\,\frac{\partial T}{\partial \mathbf{n}} = h\,(T_X - T_\infty) \tag{33}$$

with Eqn. 32, it becomes apparent that the gradient approach largely neglects significant heat transfer parameters. These parameters, however, are crucial and significantly affect heat transfer.

To illustrate this aspect, let's consider a point within a pipe that has a notable wall thickness. The point of interest is located at a distance of 3 mm from the wall within the metal-hydride bed and 50 mm from the bottom of the pipe. We will explore this scenario by examining four representative heat transfer coefficients:

$$h = \{5, 10, 25, 50, 100, 250, 500, 1000\}\ \mathrm{W/(m^2\,K)}$$

The simulation results are depicted in Fig. B.2. The gradient approach shows a negligible impact of the heat transfer coefficient on the simulation results. On the other hand, when considering the pipe wall and its associated parameters using *groovyBC*, the expected outcome is observed. Specifically, there is a proportional increase in cooling power with the heat transfer coefficient, leading to a corresponding rise in the hydrogen absorption rate.

Additionally, the gradient model predicts a stronger cooling effect, particularly noticeable when comparing the graphs for $h = 10\,\mathrm{W/(m^2\,K)}$. This emphasizes that utilizing Eqn. 32 yields more accurate results and provides better adjustability for various simulation scenarios.

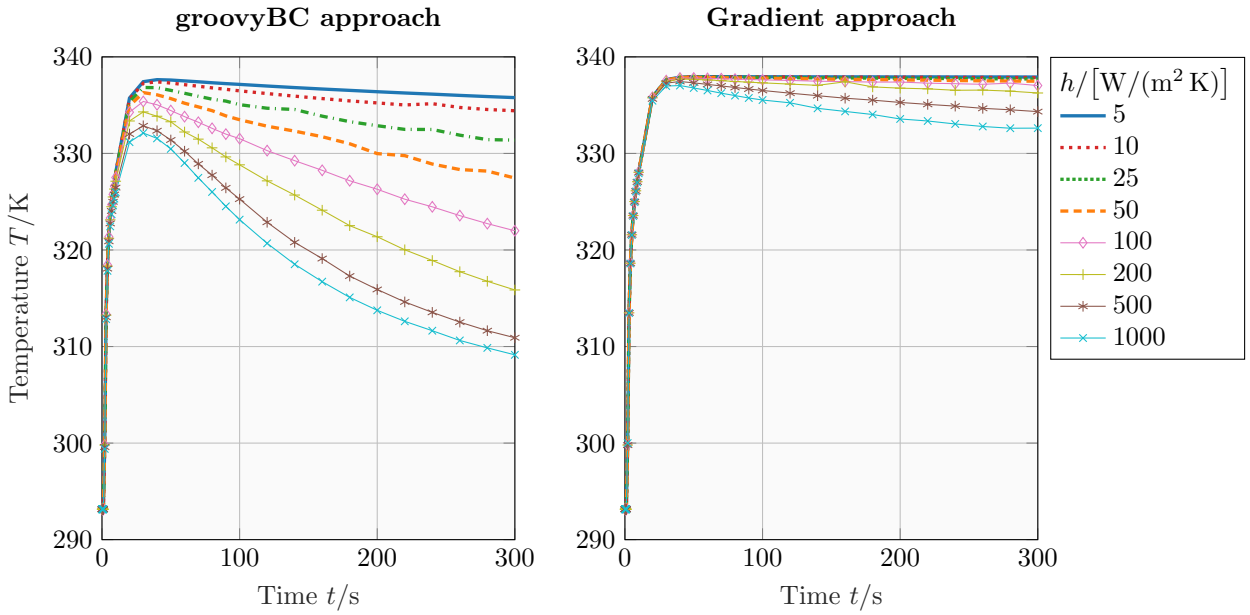

(a) Temperature T

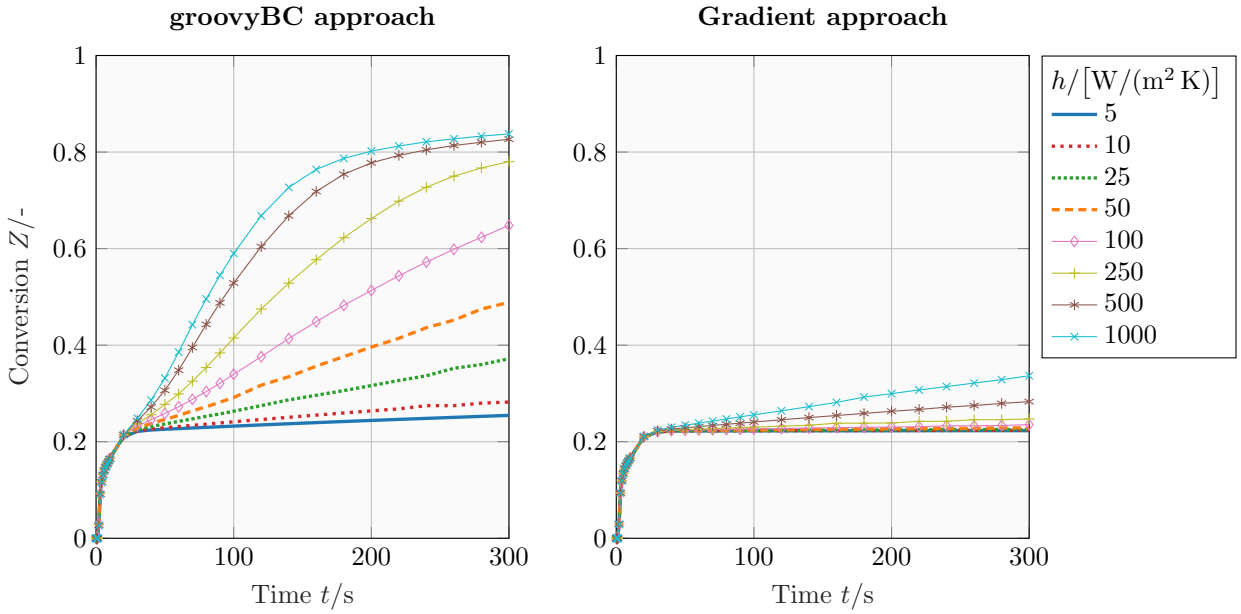

(b) Converison Z

Figure B.2. Comparison of the effect of different heat transfer coefficients on (A) the temperature and (B) the conversion near the wall

Appendix C. Boundary and Initial Conditions for the Hydrogen Area

The following section outlines the boundary and initial conditions required to set up a Hydralloy C5 absorption simulation in the *hydrogenArea*. Please note that the values provided for pressure, temperature, and velocity are intended as examples and may vary based on the specific needs of the user.

Table C.1. Pressure p – Boundary and Initial Conditions

Description	**Value**
internalField	uniform 30e5
inlet	
type	fixedValue
value	$internalField
tankWall	
type	zeroGradient
"(front | back)"	
type	wedge
hydrogenArea_to_metalArea	
type	fixedValue
value	$internalField

Table C.2. Temperature T – Boundary and Initial Conditions

Description	**Value**
internalField	uniform 293.15
inlet	
type	groovyBC
variables	k_eff=$epsilon_filter*$k_hydrogen+(1-$epsilon_filter)*$k_filter
valueExpression	293.15
gradientExpression	0
fractionExpression	1/(1+(k_eff/($h_hydrogen*mag(delta()))))
value	$internalField
tankWall	
type	groovyBC
variables	k_eff=$epsilon_filter*$k_hydrogen+(1-$epsilon_filter)*$k_filter
valueExpression	293.15
gradientExpression	0
fractionExpression	1/(1+(k_eff/($h_metal*mag(delta())))*((k_wall+h_metal*$delta_wall)/$k_wall))
value	$internalField
"(front | back)"	
type	wedge
hydrogenArea_to_metalArea	
type	zeroGradient

Appendix D. Boundary and Initial Conditions for the Metal Area

The following section depicts the Boundary and Initial Conditions in the *metalArea* to setup an Hydralloy C5 absorption simulation.

Table D.1. Pressure p – Boundary and Initial Conditions

Description	**Value**
internalField	uniform $1e5$
tankWall	
type	zeroGradient
"(front | back)"	
type	wedge
metalArea_to_hydrogenArea	
type	fixedValue
value	$internalField

Table D.2. Gas Density ρ_g – Boundary and Initial Conditions

Description	**Value**
internalField	uniform #calc "2.01588e-3 * 1e5 / (8.3145 * 293.15)"
tankWall	
type	zeroGradient
"(front | back)"	
type	wedge
metalArea_to_hydrogenArea	
type	fixedValue
value	$internalField

Table D.3. Metal Density ρ_s – Boundary and Initial Conditions

Description	**Value**
internalField	uniform 6109.6
tankWall	
type	zeroGradient
"(front | back)"	
type	wedge
metalArea_to_hydrogenArea	
type	zeroGradient

Table D.4. Temperature T – Boundary and Initial Conditions

Description	Value
internalField	uniform 293.15
	tankWall
type	groovyBC
variables	k_eff=$epsilon_metal*$k_hydrogen+(1-$epsilon_metal)*$k_metal
valueExpression	293.15
gradientExpression	0
fractionExpression	1/(1+(k_eff/($h_metal*mag(delta())))*((k_wall+h_metal*$delta_wall)/$k_wall))
value	$internalField
	"(front | back)"
type	wedge
	metalArea_to_hydrogenArea
type	fixedValue
value	$internalField

Appendix E. Numerical Schemes & Equation Solvers, Tolerances and Algorithms

In this section, we list the numerical schemes (found in *fvSchemes*) as well as the equation solvers, tolerances and algorithms (found in *fvSolution*) used for our simulations.

Table E.1. fvSchemes used in all simulations, both regions

Type	Scheme
	ddtSchemes
default	Euler
	gradSchemes
default	Gauss linear
	divSchemes
default	none
	laplacianSchemes
default	Gauss linear corrected
	interpolationSchemes
default	linear
	snGradSchemes
default	corrected

Table E.2. fvSolution used in all simulations, both regions

Type	Configuration
T, p, rho.*	
solver	PBiCGStab
preconditioner	DILU
tolerance	1e-7
relTol	0.1
nNonOrthogonalCorrectors	0

References

[1] H. Ritchie, M. Roser, and P. Rosado, "Energy," *Our World in Data*, 2022, https://ourworldindata.org/energy.

[2] BP forecasts robust global energy demand to 2030 despite efficiency gains. [Online]. Available: https://www.bp.com/en/global/corporate/news-and-insights/pressreleases/bp-forecasts-robust-global-energy-demand-to-2030-despiteefficiency-gains.html

[3] R. Busqué, R. Torres, J. Grau, V. Roda, and A. Husar, "Mathematical modeling, numerical simulation and experimental comparison of the desorption process in a metal hydride hydrogen storage system," *International Journal of Hydrogen Energy*, vol. 43, no. 35, pp. 16 929–16 940, 2018, vI Symposium on Hydrogen, Fuel Cells and Advanced Batteries – HYCELTEC 2017, 19-23 June 2017, Porto, Portugal. [Online]. Available: https://www.sciencedirect.com/science/article/pii/S0360319917348930

[4] R. A. Varin, T. Czujko, and Z. S. Wronski, *Nanomaterials for Solid State Hydrogen Storage*. Springer US, 2009. [Online]. Available: https://doi.org/10.1007/978-0-387-77712-2

[5] M. Hirscher, Ed., *Handbook of Hydrogen Storage*. Wiley, Mar. 2010. [Online]. Available: https://doi.org/10.1002/9783527629800

[6] H. Buchner, *Energiespeicherung in Metallhydriden*. Springer Vienna, 1982. [Online]. Available: https://doi.org/10.1007/978-3-7091-8671-8

[7] K. Herbrig, L. Röntzsch, C. Pohlmann, T. Weißgärber, and B. Kieback, "Hydrogen storage systems based on hydride–graphite composites: computer simulation and experimental validation," *International Journal of Hydrogen Energy*, vol. 38, no. 17, pp. 7026–7036, 2013. [Online]. Available: https://www.sciencedirect.com/science/article/pii/S0360319913007441

[8] D. Chabane, F. Harel, A. Djerdir, M. Ibrahim, D. Candusso, O. Elkedim, and N. Fenineche, "Influence of the key parameters on the dynamic behavior of the hydrogen absorption by lani5," *International Journal of Hydrogen Energy*, vol. 42, no. 2, pp. 1412–1419, 2017. [Online]. Available: https://www.sciencedirect.com/science/article/pii/S0360319916306449

[9] R. Busqué, R. Torres, J. Grau, V. Roda, and A. Husar, "Effect of metal hydride properties in hydrogen absorption through 2d-axisymmetric modeling and experimental testing in storage canisters," *International Journal of Hydrogen Energy*, vol. 42, no. 30, pp. 19 114–19 125, 2017. [Online]. Available: https://www.sciencedirect.com/science/article/pii/S0360319917324448

[10] O. Akanji and A. Kolesnikov, *Modeling of Hydrogen Absorption/Desorption in a Metal Hydride Bed Reactor — A Theoretical Study*. IntechOpen, Nov. 2015, publication Title: Advanced Materials for Renewable Hydrogen Production, Storage and Utilization. [Online]. Available: https://www.intechopen.com/chapters/undefined/state.item.id

[11] A. Chaise, P. de Rango, P. Marty, and D. Fruchart, "Experimental and numerical study of a magnesium hydride tank," *International Journal of Hydrogen Energy*, vol. 35, no. 12, pp. 6311–6322, Jun. 2010. [Online]. Available: https://doi.org/10.1016/j.ijhydene.2010.03.057

[12] Z. Bao, F. Yang, Z. Wu, X. Cao, and Z. Zhang, "Simulation studies on heat and mass transfer in high-temperature magnesium hydride reactors," *Applied Energy*, vol. 112, pp. 1181–1189, Dec. 2013. [Online]. Available: https://doi.org/10.1016/j.apenergy.2013.04.053

[13] K. Jiao, X. Li, Y. Yin, Y. Zhou, S. Yu, and Q. Du, "Effects of various operating conditions on the hydrogen absorption processes in a metal hydride tank," *Applied Energy*, vol. 94, pp. 257–269, Jun. 2012. [Online]. Available: https://doi.org/10.1016/j.apenergy.2012.01.033

[14] P. Chippar, S. D. Lewis, S. Rai, and A. Sircar, "Numerical investigation of hydrogen absorption in a stackable metal hydride reactor utilizing compartmentalization," *International Journal of Hydrogen Energy*, vol. 43, no. 16, pp. 8007–8017, Apr. 2018. [Online]. Available: https://linkinghub.elsevier.com/retrieve/pii/S0360319918307468

[15] Y. Yang, Y. Ye, J. Wei, J. Ding, and W. Wang, "Numerical Simulation on Heat Transfer and Storage Performance of Hydrogen- Heat Storage Units," Volume 2: Innovative Solutions for Energy Transitions: Part I, preprint, Feb. 2020. [Online]. Available: https://www.energy-proceedings.org/?p=1649

[16] J. Tan, M. Chai, K. He, and Y. Chen, "Numerical simulation on heating effects during hydrogen absorption in metal hydride systems for hydrogen storage," *Energies*, vol. 15, no. 7, p. 2673, Apr. 2022. [Online]. Available: https://doi.org/10.3390/en15072673

[17] K. Song and H. N. Knickle, "Time dependent analysis of a metal hydride bed," *ECS Transactions*, vol. 19, no. 10, pp. 41–56, Oct. 2009. [Online]. Available: https://doi.org/10.1149/1.3237107

[18] B. MACDONALD and A. ROWE, "Impacts of external heat transfer enhancements on metal hydride storage tanks," *International Journal of Hydrogen Energy*, vol. 31, no. 12, pp. 1721–1731, Sep. 2006. [Online]. Available: https://doi.org/10.1016/j.ijhydene.2006.01.007

[19] E. I. Gkanas, "Metal hydrides: Modeling of metal hydrides to be operated in a fuel cell," in *Portable Hydrogen Energy Systems*. Elsevier, 2018, pp. 67–90. [Online]. Available: https://doi.org/10.1016/b978-0-12-813128-2.00005-x

[20] K. Couturier, F. Joppich, A. Wo¨rner, and R. Tamme, "Tank Design for On-Board Hydrogen Storage in Metal Hydrides," in *ASME 2008 2nd International Conference on Energy Sustainability, Volume 1*. Jacksonville, Florida, USA: ASMEDC, Jan. 2008, pp. 517–524. [Online]. Available: https://asmedigitalcollection.asme.org/ES/proceedings/ES2008/43192/517/322651

[21] A. Chibani, C. Bougriou, and S. Merouani, "Simulation of hydrogen absorption/desorption on metal hydride LaNi5-H2: Mass and heat transfer," *Applied Thermal Engineering*, vol. 142, pp. 110–117, Sep. 2018. [Online]. Available: https://linkinghub.elsevier.com/retrieve/pii/S1359431118310834

[22] F. Askri, M. Ben Salah, A. Jemni, and S. Ben Nasrallah, "Heat and mass transfer studies on metal-hydrogen reactor filled with MmNi4.6Fe0.4," *International Journal of Hydrogen Energy*, vol. 34, no. 16, pp. 6705–6711, Aug. 2009. [Online]. Available: https://linkinghub.elsevier.com/retrieve/pii/S0360319909009707

[23] A. Jemni, S. B. Nasrallah, and J. Lamloumi, "Experimental and theoretical study of ametal–hydrogen reactor," *International Journal of Hydrogen Energy*, vol. 24, no. 7, pp. 631–644, Jul. 1999. [Online]. Available: https://linkinghub.elsevier.com/retrieve/pii/S0360319998001177

[24] J. Nam, J. Ko, and H. Ju, "Three-dimensional modeling and simulation of hydrogen absorption in metal hydride hydrogen storage vessels," *Applied Energy*, vol. 89, no. 1, pp. 164–175, Jan. 2012. [Online]. Available: https://doi.org/10.1016/j.apenergy.2011.06.015

[25] X. Lin, H. Yang, Q. Zhu, and Q. Li, "Numerical simulation of a metal hydride tank with LaNi4.25Al0.75 using a novel kinetic model at constant flows," *Chemical Engineering Journal*, vol. 401, p. 126115, Dec. 2020. [Online]. Available: https://linkinghub.elsevier.com/retrieve/pii/S1385894720322439

[26] A. Demircan, M. Demiralp, Y. Kaplan, M. Mat, and T. Veziroglu, "Experimental and theoretical analysis of hydrogen absorption in lani5–h2 reactors," *International Journal of Hydrogen Energy*, vol. 30, no. 13, pp. 1437–1446, 2005. [Online]. Available: https://www.sciencedirect.com/science/article/pii/S0360319905000376

[27] M. S. Manai, M. Leturia, C. Pohlmann, J. Oubraham, S. Mottelet, M. Levy, and K. Saleh, "Comparative study of different storage bed designs of a solid-state hydrogen tank," *Journal of Energy Storage*, vol. 26, p. 101024, Dec. 2019. [Online]. Available: https://doi.org/10.1016/j.est.2019.101024

[28] F. Askri, M. Bensalah, A. Jemni, and S. Bennasrallah, "Optimization of hydrogen storage in metal-hydride tanks," *International Journal of Hydrogen Energy*, vol. 34, no. 2, pp. 897–905, Jan. 2009. [Online]. Available: https://linkinghub.elsevier.com/retrieve/pii/S0360319908014778

[29] H. Dhaou, F. Askri, M. Ben Salah, A. Jemni, S. Ben Nasrallah, and J. Lamloumi, "Measurement and modelling of kinetics of hydrogen sorption by lani5 and two related pseudobinary compounds," *International Journal of Hydrogen Energy*, vol. 32, no. 5, pp. 576–587, 2007. [Online]. Available: https://www.sciencedirect.com/science/article/pii/S0360319906002783

[30] C. He, Y. Wang, J. Song, S. Li, F. Yang, Z. Wu, L. Zheng, Z. Zhang, and K. Kim, "Design optimization of autoswitch hydrogen absorption and desorption device using metal hydrides," *International Journal of Chemical Reactor Engineering*, vol. 15, no. 6, p. 20160180, 2017. [Online]. Available: https://doi.org/10.1515/ijcre-2016-0180

[31] A. Boukhari, "Numerical investigation of heat and mass transfer processes while the desorption of hydrogen gas stored in MmNi4.6fe0.4-h6," *International Journal of Energetica*, vol. 1, no. 1, p. 1, Dec. 2016. [Online]. Available: https://doi.org/10.47238/ijeca.v1i1.5

[32] M. Bedrunka, N. Bornemann, G. Steinebach, and D. Reith, "Reaction behavior modeling of metal hydride based on FeTiMn using numerical simulations," Jan. 2021, preprint submitted to Journal of Elsevier. [Online]. Available: https://doi.org/10.31224/osf.io/ak8j3

[33] Y. Zhuo, S. Jung, and Y. Shen, "Numerical study of hydrogen desorption in an innovative metal hydride hydrogen storage tank," *Energy Fuels*, vol. 35, no. 13, pp. 10 908–10 917, Jun. 2021. [Online]. Available: https://doi.org/10.1021/acs.energyfuels.1c00666

[34] A. A. R. Darzi, H. H. Afrouzi, A. Moshfegh, and M. Farhadi, "Absorption and desorption of hydrogen in long metal hydride tank equipped with phase change material jacket," *International Journal of Hydrogen Energy*, vol. 41, no. 22, pp. 9595–9610, Jun. 2016. [Online]. Available: https://doi.org/10.1016/j.ijhydene.2016.04.051

[35] A. K. Phate, M. P. Maiya, and S. S. Murthy, "Simulation of transient heat and mass transfer during hydrogen sorption in cylindrical metal hydride beds," *International Journal of Hydrogen Energy*, vol. 32, no. 12, pp. 1969–1981, Aug. 2007. [Online]. Available: https://doi.org/10.1016/j.ijhydene.2006.09.020

[36] A. Freni, F. Cipitì, and G. Cacciola, "Finite element-based simulation of a metal hydride-based hydrogen storage tank," *International Journal of Hydrogen Energy*, vol. 34, no. 20, pp. 8574–8582, Oct. 2009. [Online]. Available: https://doi.org/10.1016/j.ijhydene.2009.07.118

[37] B. F. Gschaider, "Contrib/groovyBC - OpenFOAMWiki," Feb. 2009. [Online]. Available: https://openfoamwiki.net/index.php/Contrib_groovyBC

[38] A. Schweizer. Wärmeleitfähigkeit von metallen. [Online]. Available: https://www.schweizer-fn.de/stoff/wleit_metall/wleit_metall.php

[39] E. AG. Eigenschaften von porösem aluminium. [Online]. Available: https://www.exxentis.com/poroeses-aluminium/eigenschaften/

[40] V. SKRIPNYUK and M. RON, "Hydrogen desorption kinetics in intermetallic compounds c2, c5 and c5 with laves phase structure," *International Journal of Hydrogen Energy*, vol. 28, no. 3, pp. 303–309, Mar. 2003. [Online]. Available: https://doi.org/10.1016/s0360-3199(02)00081-2

[41] Chemical portal - chemistry online education. [Online]. Available: http://www.webqc.org/

[42] K. Lahmer, R. Bessaïh, A. Scipioni, and M. El Ganaoui, "Thermal modeling of hydrogen storage by absorption in a magnesium hydrides tank," *Int. J. Simul. Multidisci. Des. Optim.*, vol. 5, p. A21, 2014. [Online]. Available: http://www.ijsmdo.org/10.1051/smdo/2014002

[43] P. Larpruenrudee, N. S. Bennett, Y. Gu, R. Fitch, and M. S. Islam, "Design optimization of a magnesium-based metal hydride hydrogen energy storage system," *Scientific Reports*, vol. 12, no. 1, Aug. 2022. [Online]. Available: https://doi.org/10.1038/s41598-022-17120-3

[44] X. Lin, D. Sun, S. Chen, Q. Zhu, H. Leng, and Q. Li, "Numerical analysis on pulverization and self-densification for hydrogen storage performance of a metal hydride tank," *Applied Thermal Engineering*, vol. 161, p. 114129, Oct. 2019. [Online]. Available: https://doi.org/10.1016/j.applthermaleng.2019.114129

[45] E. HAHNE, "Thermal conductivity of metal hydride materials for storage of hydrogen: Experimental investigation," *International Journal of Hydrogen Energy*, vol. 23, no. 2, pp. 107–114, Feb. 1998. [Online]. Available: https://doi.org/10.1016/s0360-3199(97)00020-7

[46] T. O. Saetre, Ed., *Hydrogen Power: Theoretical and Engineering Solutions*. Springer Netherlands, 1998. [Online]. Available: https://doi.org/10.1007/978-94-015-9054-9

[47] S. Singh and V. Ramadesigan, Eds., *Advances in Energy Research, Vol. 1*. Springer Singapore, 2020. [Online]. Available: https://doi.org/10.1007/978-981-15-2666-4

[48] P. Muthukumar and S. V. Ramana, "Numerical simulation of coupled heat and mass transfer in metal hydride-based hydrogen storage reactor," *Journal of Alloys and Compounds*, vol. 472, no. 1-2, pp. 466–472, Mar. 2009. [Online]. Available: https://doi.org/10.1016/j.jallcom.2008.04.088

[49] P. Kosky, R. Balmer, W. Keat, and G. Wise, "Mechanical engineering," in *Exploring Engineering*. Elsevier, 2021, pp. 317–340. [Online]. Available: https://doi.org/10.1016/b978-0-12-815073-3.00014-4

[50] A. Dybbs and R. V. Edwards, *Fundamentals of Transport Phenomena in Porous Media*, J. Bear and M. Y. Corapcioglu, Eds. Dordrecht: Springer Netherlands, 1984. [Online]. Available: http://link.springer.com/10.1007/978-94-009-6175-3

[51] M. Tek, "Development of a Generalized Darcy Equation," *Journal of Petroleum Technology*, vol. 9, no. 06, pp. 45–47, Jun. 1957. [Online]. Available: https://onepetro.org/JPT/article/9/06/45/160954/Development-of-a-Generalized-Darcy-Equation

[52] P. Kundu, V. Kumar, and I. M. Mishra, "Experimental and numerical investigation of fluid flow hydrodynamics in porous media: Characterization of pre-Darcy, Darcy and non-Darcy flow regimes," *Powder Technology*, vol. 303, pp. 278–291, Dec. 2016. [Online]. Available: https://linkinghub.elsevier.com/retrieve/pii/S0032591016306209

[53] J. Comiti, N. Sabiri, and A. Montillet, "Experimental characterization of flow regimes in various porous media — III: limit of Darcy's or creeping flow regime for Newtonian and purely viscous non-Newtonian fluids," *Chemical Engineering Science*, vol. 55, no. 15, pp. 3057–3061, Aug. 2000. [Online]. Available: https://linkinghub.elsevier.com/retrieve/pii/S0009250999005564

[54] C. Chung, Y.-Z. Chen, Y.-P. Chen, and M.-S. Chang, "CFD investigation on performance enhancement of metal hydride hydrogen storage vessels using heat pipes," *Applied Thermal Engineering*, vol. 91, pp. 434–446, Dec. 2015. [Online]. Available: https://doi.org/10.1016/j.applthermaleng.2015.08.039

[55] S. Nasrallah, "Heat and mass transfer models in metal-hydrogen reactor," *International Journal of Hydrogen Energy*, vol. 22, no. 1, pp. 67–76, Jan. 1997. [Online]. Available: https://linkinghub.elsevier.com/retrieve/pii/S0360319996000390

[56] A. R. Velasco, "Boundary conditions for convetive heat transfer in OpenFOAM." [Online]. Available: https://foamingtime2.files.wordpress.com/2017/07/convection-bc_1.pdf

[57] R. Vilums, "Implementation of transient robin boundary conditions in OpenFOAM." [Online]. Available: http://www.modlab.lv/docs/2011/OpenFOAM/Abstracts_R_Vilums_pdf.pdf